3
Understanding the Metal–Molecule Interface from First Principles

Leeor Kronik and Yoshitada Morikawa

3.1
Introduction

It is by now well-established that the molecule–metal interface can possess a range of surprising electronic properties that are of intense interest from both the basic science and applied research points of view. Indeed, this is emphasized throughout this book. Identifying and understanding these new properties is a very significant challenge not just for experiment, but also for theory. To a large extent, this is because considering the molecule–metal interface properties forces us to bridge two different "world views" – that of molecular orbital theory, which underlies much of organic chemistry, and that of delocalized electron waves, which underlies much of solid-state physics [1, 2]. One often encounters phenomena that are not well-described by either of the limiting textbook descriptions, and more elaborate theories need to be constructed. Bridging between the two limiting cases so as to form a coherent phenomenological framework is already difficult, but the challenge here is in fact significantly larger due to the possible emergence of "collective effects" at the interface.

We define collective effects as phenomena that the individual components comprising the interface (say a single molecule or the isolated metallic substrate) do not exhibit [2, 3]. Perhaps the most striking example of such a collective effect is the emergence of magnetic phenomena at the interface between a nonmagnetic metal and a closed-shell molecular layer [4]. But there are many other examples. One such phenomenon is the emergence of qualitatively new electronic states at the interface [5–7], due to hybridization of metallic and molecular orbitals. Such hybridization can even result in the induction of magnetic phenomena from metal to molecule, or vice versa [8–10]. Another phenomenon involves the appearance of interface-localized electron–hole pairs (sometimes referred to as "charge transfer" or "hybrid" excitons) [11–13]. Furthermore, by no means is direct chemical interaction necessary for collective phenomena to occur. For example, long-range electrostatic effects can drastically affect the static polarization in, and electric fields outside of, a molecular monolayer [14, 15]. Consequently, properties of the molec-

The Molecule–Metal Interface, First Edition. Edited by N. Koch, N. Ueno, and A.T.S. Wee.
© 2013 WILEY-VCH Verlag GmbH & Co. KGaA. Published 2013 by WILEY-VCH Verlag GmbH & Co. KGaA.

ular ensemble, as well as of its interface with the metal, can be very different from, and sometimes even opposite to [16], those of the isolated molecule. Similarly, intermolecular interaction, which may additionally be substrate mediated, can have profound effects on the transport through a molecular layer [17, 18]. Furthermore, dynamic polarization effects, arising from both the molecular environment and the metallic one, can renormalize the energy of frontier orbitals [19], again changing both spectroscopic properties and transport behavior significantly.

Untangling the web of short-range chemical bonds, long-range electrostatic and dispersive interactions, and intermolecular and molecule–substrate interplay presents significant challenges. This is all the more so given that one has not only to understand general mechanisms that may allow for collective behavior, but also rationalize how these depend on system-specific properties such as bonding, order, and orientation, and understand when and how they may arise.

The theoretical framework best-suited for circumventing these difficulties is first principles electronic structure theory, where electronic and optical properties are ideally deduced from nothing but the atomic species present and the laws of quantum physics [20, 21]. Quite generally, such theory can be useful at three different levels: confirmation, interpretation, and prediction. The lowest level, confirmation, is needed because cutting-edge materials science often involves materials whose formation is not always fully controlled and whose properties are not always fully characterized. Experimental results may then be controversial and using experiment alone as a guide could be misleading. Reproduction of the experimental result by means of a calculation that did not rely on any experimentally derived quantities can then serve as strong evidence for the veracity of the experimental result. Interpretation is then the next logical step – sufficiently accurate calculations, compared with pertinent experiments, can then be a strong driver towards the construction and examination of new concepts, phenomenological models, and so on. This is especially so given that on the computer it is possible to access the energy and orbital of each electron, and to perform tasks that would be very difficult to outright impossible experimentally, such as: removing a metallic substrate while keeping a molecular overlayer ordered; changing the adsorption geometry; moving, adding, or removing a single atom; and so on. At the highest level comes prediction: because they do not require experimental input, accurate first principles calculations can be an invaluable tool for rational design and property evaluation of materials systems, even if they were never synthesized. Thus, theory can guide which experimental efforts (which can be highly time and capital consuming) are actually worth embarking upon.

By far the most common first principles electronic structure theory is density functional theory (DFT) [22–25]. DFT is an approach to the many-electron problem in which the electron density, rather than the many-electron wavefunction, plays the central role. In recent years, DFT has become the method of choice for electronic structure calculations across an unusually wide variety of fields, from organic chemistry to condensed matter physics. There are two main reasons for the success of DFT. First, it offers the only currently known practical method for routinely performing fully quantum mechanical calculations for systems with many

hundreds or even thousands of electrons. Second, it enhances our understanding by relying on relatively simple, physically accessible quantities that are easily visualized even for very large systems.

Unfortunately, a very serious disadvantage of DFT is that while the above-mentioned mapping is exact in principle, it is always approximate in practice. This is because relying on the electron density requires a "mapping functional" that is only approximately known. Thus, while there is very much that present-day DFT (namely, DFT with currently prevalent approximate functionals) already describes correctly, there are also important quantities it does not capture correctly. In particular, and as discussed in detail below, several important generic properties of the metal–molecule interface are difficult to capture with present-day DFT.

Fortunately, recent progress with DFT formalism, assessment, and application has led to significant progress in the range of issues which can be addressed using DFT, and has already led to many interesting insights in the study of metal–molecule interfaces. In this chapter, we survey the progress made, discuss remaining open issues, and provide specific examples of successful first principles studies of metal–molecule interfaces. The chapter is arranged as follows. First, we briefly introduce the basic formalism of DFT and discuss commonly employed approximate functionals. Next, we discuss issues of particular importance for the electronic structure of metal–molecule interfaces and how they are reflected in different functionals. Finally, we overview recent studies of the interface between prototypical metals and prototypical molecules useful in organic electronics, progressing from weakly adsorbed molecules to strongly adsorbed ones. At each step, we emphasize the insights obtained from state-of-the-art first principles methods.

3.2
A Brief Overview of Density Functional Theory

The central tenet of DFT is the Hohenberg–Kohn theorem [26], which states that the ground state density $n(\boldsymbol{r})$ of a system of interacting electrons subject to some external potential $v_{\text{ext}}(\boldsymbol{r})$ determines this potential uniquely (up to a physically trivial constant). The importance of this theorem lies in the fact that (within the Born–Oppenheimer approximation) any atomic, molecular, or condensed matter system is completely described by the number of electrons in it, which is simply an integral of $n(\boldsymbol{r})$ over space, and by the types and positions of the nuclei in it. The effect of the latter two quantities on the electron system is given completely by the ion–electron attraction potential. This potential is external to the electron system and therefore, according to the Hohenberg–Kohn theorem, is uniquely determined by the ground state density. This means that the ground state density contains all the information needed to describe the system completely and uniquely.

The above considerations are typically not employed directly, but rather are used in the construction of the Kohn–Sham equation [27], which is the "workhorse" of DFT. In Kohn–Sham DFT, the original interacting electron Schrödinger equation is mapped into an equivalent noninteracting problem, such that the ground state

density of the noninteracting system is equal to that of the original system. This leads to effective one-particle equations, which in spin-polarized form are given by:

$$\left(-\frac{\hbar^2\nabla^2}{2m} + v_{\text{ext}}(\boldsymbol{r}) + v_{\text{H}}([n];\boldsymbol{r}) + v_{\text{xc},\sigma}([n_\uparrow, n_\downarrow];\boldsymbol{r})\right)\varphi_{i,\sigma}(\boldsymbol{r}) = \varepsilon_{i,\sigma}\varphi_{i,\sigma}(\boldsymbol{r}) \tag{3.1}$$

where $\sigma = \uparrow$ or $\downarrow$ is the electron spin z-component index, $\hbar$ is the reduced Planck constant, m is the electron mass, $\varepsilon_{i,\sigma}$ and $\varphi_{i,\sigma}$ are known as Kohn–Sham energies and orbitals, respectively, $n_\sigma(\boldsymbol{r})$ is the electron density of spin σ, which is calculated as a sum over filled orbitals:

$$n_\sigma(\boldsymbol{r}) = \sum_{i=1}^{N_\sigma} |\varphi_{i,\sigma}(\boldsymbol{r})|^2 \tag{3.2}$$

with $n(\boldsymbol{r}) = n_\uparrow(\boldsymbol{r}) + n_\downarrow(\boldsymbol{r})$, and N_σ the number of filled orbitals of spin σ. The term $v_{\text{H}}([n];\boldsymbol{r}) = e^2 \int d^3r' n(\boldsymbol{r}')/|\boldsymbol{r} - \boldsymbol{r}'|$ is the Hartree potential, which describes the classical electron–electron Coulomb repulsion, and $v_{\text{xc},\sigma}([n_\uparrow, n_\downarrow];\boldsymbol{r})$ is the (spin-dependent) exchange–correlation potential, which includes all nonclassical electron interactions, namely, Pauli exchange, electron correlation, and the difference between the kinetic energy of the interacting and noninteracting electron systems. The exchange–correlation potential can be expressed as a functional derivative of the exchange–correlation energy, $E_{\text{xc}}([n_\uparrow, n_\downarrow])$, namely

$$v_{\text{xc},\sigma}([n_\uparrow, n_\downarrow];\boldsymbol{r}) \equiv \frac{\delta E_{\text{xc}}}{\delta n_\sigma(\boldsymbol{r})} \tag{3.3}$$

Unfortunately, the exact form of E_{xc}, and consequently v_{xc}, is not known. This is not surprising, given that it has to reflect the full complexity of the original many-body problem. The practical success of DFT therefore hinges entirely on the existence of suitable approximations for E_{xc}.

An early, appealingly simple approximation for the exchange–correlation energy functional, already suggested by Kohn and Sham [27], is the local density approximation (LDA), or, in its spin-polarized form, the local spin density approximation (LSDA). In this approximation, we assume that at each point in space the exchange–correlation energy per particle is given by its value for a homogeneous electron gas, $e_{\text{xc}}(n_\uparrow(\boldsymbol{r}), n_\downarrow(\boldsymbol{r}))$, namely

$$E_{\text{xc}}^{\text{LSDA}}[n_\uparrow, n_\downarrow] = \int d^3r\, n(\boldsymbol{r}) e_{\text{xc}}(n_\uparrow(\boldsymbol{r}), n_\downarrow(\boldsymbol{r})) \tag{3.4}$$

This approximation has several advantages. First, $e_{\text{xc}}(n_\uparrow(\boldsymbol{r}), n_\downarrow(\boldsymbol{r}))$ is unique, because of the theoretical existence of a system with uniform spin densities. Second, e_{xc} has been known approximately already when Hohenberg, Kohn, and Sham were formulating DFT, and has since been computed more accurately using Monte Carlo methods [28]. Furthermore, several useful analytical parametrization of the Monte Carlo results that also take into account other known limits and/or scaling

laws of e_{xc}, have been given [29–31]. Last but not least, the exchange–correlation potential, given by Eq. (3.3), becomes a simple *function*, rather than a functional, of $n_\uparrow(\boldsymbol{r})$ and $n_\downarrow(\boldsymbol{r})$. The difficulty with L(S)DA is that in real systems the density is clearly not uniform. More often than not, it actually exhibits rapid changes in space. L(S)DA was therefore expected to be of limited value in providing an accurate description of the electron interaction [27]. Nevertheless, it has often been found to provide surprisingly accurate predictions of experimental results (see, e.g., [32]), partly due to a systematic cancellation of errors between the exchange and correlation terms.

Despite its numerous successes, L(S)DA is by no means a panacea. Even when its predictions are qualitatively acceptable (which is not always the case, as shown below), L(S)DA is far from perfect quantitatively. L(S)DA tends to overestimate the bonding strength, resulting in bond lengths that are too short by several percent. It also provides an absolute error of molecular atomization energies of the order of 1 eV – much larger than the desired "chemical accuracy" of roughly 0.05 eV [33].

Many of these quantitative failures of L(S)DA are remedied, or at least greatly reduced, by using the generalized gradient approximation (GGA) for the exchange–correlation energy [33]:

$$E_{xc}^{GGA}[n_\uparrow(\boldsymbol{r}), n_\downarrow(\boldsymbol{r})] = \int d^3r\, f(n_\uparrow(\boldsymbol{r}), n_\downarrow(\boldsymbol{r}), \nabla n_\uparrow(\boldsymbol{r}), \nabla n_\downarrow(\boldsymbol{r})) \tag{3.5}$$

GGA is often dubbed a "semilocal" approximation of the exchange–correlation energy. It is no longer strictly local like L(S)DA, but includes information on deviations from homogeneity only by considering the gradients of the spin-polarized charge densities. It is called a "generalized" gradient approximation because the function $f(\cdot)$ in Eq. (3.5) is not obtained from a simple gradient expansion of E_{xc}. This is because unlike L(S)DA, which is derived from a possible (though highly idealized) physical system, a simple gradient expansion is not. It therefore does not obey many formal properties of the exact E_{xc} that L(S)DA does and ergo its accuracy is often miserable.

Instead, $f(\cdot)$ in Eq. (3.5) is constructed so as to reproduce many important formal properties of the exact functional, for example, the exact result in certain limits and correct scaling with respect to the density [34]. Alternatively, it can be derived semiempirically by choosing a reasonable form and fitting the remaining parameters to a known data set, typically of thermochemical properties [35]. Use of GGA functionals constructed in either of the two ways indeed often offers a significantly improved quantitative agreement with experiment. For example, it corrects (often a bit overcorrects) for the L(S)DA overestimate of bonding strength, does not overly favor close-packed structures, and provides an absolute error of molecular atomization energies of the order of 0.3 eV. This is still above the desired "chemical accuracy," but much better than L(S)DA [33].

Beyond GGA, by far the most popular choice is that of hybrid functionals [36]. Generally, hybrid functionals incorporate a fraction of exact exchange energy, de-

fined in terms of the Fock integral,

$$E_{\mathrm{x}}^{\mathrm{exact}} = -\frac{e^2}{2} \sum_{\sigma=\uparrow,\downarrow} \sum_{i,j=1}^{N_\sigma} \iint \frac{\varphi_{i,\sigma}^*(\boldsymbol{r})\varphi_{j,\sigma}^*(\boldsymbol{r}')\varphi_{j,\sigma}(\boldsymbol{r})\varphi_{i,\sigma}(\boldsymbol{r}')}{|\boldsymbol{r}-\boldsymbol{r}'|} d^3r' d^3r \tag{3.6}$$

which is familiar from Hartree–Fock theory. The exchange–correlation energy is then expressed as

$$E_{\mathrm{xc}}^{\mathrm{hyb}} = b\, E_x^{\mathrm{exact}} + (1-b)\, E_x^{\mathrm{app}} + E_c^{\mathrm{app}} \tag{3.7}$$

where b is the exact exchange fraction and the superscripts "hyb" and "app" denote the hybrid functional and the approximate (typically semilocal) exchange and correlation functionals from which it is constructed. As with GGA functionals, hybrid functionals can be constructed either nonempirically or semiempirically. In the nonempirical PBE (Perdew, Burke, Ernzerhof) hybrid (PBEh) functional, E_x^{app} and E_c^{app} are taken as are from the GGA-PBE functional. Therefore b is the only free parameter and it is determined from nonempirical considerations. In the semiempirical functional B3LYP (Becke exchange, 3 Parameters, Lee–Yang–Parr correlation) [37], the fraction of exact exchange, as well as two additional parameters in the underlying GGA expressions (hence the "3" in the functional name) are left free and are determined by fitting to thermochemical data.

Almost invariably, with hybrid functionals one does not construct the potential from the energy using Eq. (3.3), that is, by taking a functional derivative with respect to the density. Rather, because the Fock-exchange depends explicitly on the orbitals, the energy is derived with respect to the latter, leading to a nonlocal, Fock-operator potential. The name "hybrid functionals" is derived from this property, because these functionals appear to be a mixture of the Kohn–Sham and Hartree–Fock world views. A more modern perspective is to view such nonlocal potential operators as belonging to a *generalized* Kohn–Sham equation – one that is obtained by mapping the interacting electron system into a system of partially interacting electrons that can still be represented by a single Slater determinant [38]. Thus, hybrid functionals are outside of the Kohn–Sham construct, but still well within formal DFT [36, 39, 40].

Hybrid functionals have gained enormous popularity in organic chemistry in particular, because they offer a further and significant reduction of errors with respect to GGA functionals. For example, for the formation enthalpies of the G3 set of thermochemical data, the mean error is 0.94 eV with PBE-GGA, but only 0.2 eV with the PBE-based hybrid, PBEh, and 0.15 eV with B3LYP, respectively [41]. From a fundamental point of view, there are several perspectives to rationalize why one would wish to use a fraction of exact exchange, rather than all of it [36]. For our purposes here, it suffices to note that full exact exchange would necessarily require a highly nonlocal correlation expression, which at present is unknown. Retaining only a fraction of it provides for a reasonable balance between enjoying its advantages and retaining a simple, semilocal correlation functional.

In an even more recent class of functionals, gaining additional flexibility in the functional form is obtained by partitioning the exchange term into short-range (SR)

and long-range (LR) parts. This is achieved by means of splitting the Coulomb repulsion term between electrons i and j into SR and LR components, for example according to [42]

$$\frac{1}{|\boldsymbol{r}_i - \boldsymbol{r}_j|} = \frac{\mathrm{erf}(\mu|\boldsymbol{r}_i - \boldsymbol{r}_j|)}{|\boldsymbol{r}_i - \boldsymbol{r}_j|} + \frac{1 - \mathrm{erf}(\mu|\boldsymbol{r}_i - \boldsymbol{r}_j|)}{|\boldsymbol{r}_i - \boldsymbol{r}_j|} \tag{3.8}$$

where erf(·) denotes the standard error function and μ is the range-separation parameter. One can then construct both exact and semilocal exchange from the SR part and the LR part separately, and generalize the hybridization scheme by invoking different weights for the short-range and the long-range exact exchange. Such generalization of the above conventional hybrid, Eq. (3.7), yields [36]:

$$E_{\mathrm{xc}}^{\mathrm{hyb}} = a\, E_x^{\text{SR-exact}} + (1-a)\, E_x^{\text{SR-app}} + b\, E_x^{\text{LR-exact}} + (1-b)\, E_x^{\text{LR-app}} + E_c^{\mathrm{app}} \tag{3.9}$$

One useful limit of Eq. (3.9) is obtained by setting $b = 0$, that is, by excluding the long-range portion of the exact exchange altogether [43, 44]. The obtained "screened hybrid" greatly facilitates calculations with hybrid functionals in solids, at no significant sacrifice of accuracy, because the computational effort associated with the slow long-range decay of the exchange integral is eliminated [45]. The best-known functional of this kind is the HSE one, which is the short-range version of PBEh, with μ determined semiempirically [45, 46]. The opposite limit, $b = 1$, is often useful for finite systems, because it enforces the correct asymptotic behavior of the exchange potential [40], and is discussed further below.

Having discussed some useful functionals, it is important to make some general remarks about the physical meaning of Kohn–Sham eigenvalues and orbitals, which are discussed at length below. The (occupied) Kohn–Sham orbitals and their eigenvalues were originally introduced as mere mathematical devices, to be used so as to obtain the correct ground state density. Therefore, in the early days of density functional theory it has been believed that no physical meaning whatsoever should be attached to them. Only the highest occupied eigenvalue can be assigned with a rigorous physical meaning: for this special case, the eigenvalue should be equal and opposite to the ionization potential (a condition often not obeyed by approximate density functionals) [47, 48]. Nevertheless, interpreting Kohn–Sham eigenvalues and orbitals as if they were true one-electron excitation energies and orbitals often results in surprisingly accurate results [36]. Relatively recent research has shown that Kohn–Sham eigenvalues are in fact approximations to relaxed electron removal energies [49]. For exact exchange–correlation potentials, reconstructed from charge densities determined by wavefunction-based methods for several small molecules, the higher lying eigenvalues were found to be within ~ 0.1 eV of exact photoionization energies [50]. Similarly, Kohn–Sham orbitals can be viewed as valid one-electron molecular orbitals for use in qualitative traditional chemical analysis. Furthermore, they often quantitatively mimic quasi-particle single-electron wavefunctions [51, 52], the latter being rigorously defined one-electron orbitals, indicative of electron removal/insertion.

Finally, for understanding the metal–molecule interface one frequently has to capture accurately interactions with significant noncovalent interactions – notably

van der Waals interactions, but also hydrogen bonds. Unfortunately, such treatment is absent by construction from all functionals we have surveyed so far. The reason is that from the DFT point of view, such interactions must involve nonlocal, long-range correlation expressions that none of the above-surveyed functionals possess.

Many strategies toward inclusion of van der Waals interactions in DFT calculations, at various levels of approximation, have been proposed. Of those, two have become popular in the study of metal–molecule interfaces as they could afford a reasonable balance between accuracy and computational complexity. The first attacks the correlation problem "head-on," by introducing explicit long-range correlation that is integrated with traditional exchange–correlation functionals. The most practical and successful representative of this first strategy is the "vdW-DFT" functional of Dion *et al.* [53] and variants thereof (see, e.g., [54–56]). In this approach, the main challenge is to determine appropriate long-range correlation expressions that would correctly capture various scenarios of van der Waals attraction, without upsetting the delicate balance between short- and medium-range exchange and correlation contributions.

The second popular strategy does not attack the correlation problem directly, but rather circumvents it by adding pairwise, C_6/R^6 corrections to the internuclear energy expression, damped in the short-range while providing the desired long-range asymptotic behavior. Such corrections are usually semiempirical, but can also be derived from first-principles considerations. The most popular representatives of this approach are Grimme's "DFT-D" corrections [57, 58] and the Tkatchenko–Scheffler "minimally empirical" approach [59]. To be useful, the pairwise coefficients must be adapted to the chemical environment. In Grimme's approach, this is done by chemical hybridization considerations, whereas in the Tkatchenko–Scheffler approach this is achieved from physical considerations involving normalization of the relative polarizability of an atom inside its chemical environment. Clearly the main challenge in such approaches is the construction of sufficiently accurate and general pairwise coefficients and damping function, as well as the consideration of screening phenomena that are beyond pairwise corrections [60]. A major advantage, however, is that such pairwise corrections can in principle be adapted to any underbinding exchange–correlation functional and consequently the thorny problem of obtaining a description of both geometry and electronic structure can be largely overcome by decoupling the two issues [61, 62].

We note in passing that in organic chemistry a third popular strategy is the use of semiempirically parameterized exchange–correlation functionals, calibrated for data sets that include noncovalently interacting systems. The most popular representative of this approach is the M06 family of functionals [63, 64]. The training data sets typically do not include metals and not many applications of this approach to the metal–molecule interface have been reported [65]. We therefore do not discuss this approach further here.

While the above survey is by no means comprehensive, it is sufficient for understanding how the pros and cons of the various functionals affect computations of

metal–molecule interfaces, with an emphasis on the electronic structure, which is the next topic of our discussion.

3.3
Electronic Structure of Metal–Molecule Interfaces from Density Functional Theory: Challenges and Progress

A major challenge of first principles studies of molecule–metal interfaces is the need to use an approximate exchange–correlation density functional that provides equally accurate predictions across both sides of the interface. We have previously discussed the accuracy gained, across canonical molecular data sets, by making the transition from a GGA functional to a hybrid functional. The opposite, however, is true for, e.g., atomization energies in the solid. Whereas the mean absolute relative error with PBE is a reasonable 3.4%, it grows to 7.4% for PBEh and to 17.6% for B3LYP [66]. These numbers likely paint an overly bleak picture, because other properties of interest for molecule–metal interfaces, for example, adsorption geometry, are typically not as sensitive to the underlying functional. Nevertheless, this does establish a fundamental challenge associated with describing two very different materials groups on the same footing.

Importantly, molecular and metallic systems also place opposite constraints on the electronic structure obtained with different exchange–correlation functionals. To understand why, consider the prototypical case of the valence electronic structure of gas phase 3,4,9,10-perylene tetracarboxylic dianhydride (PTCDA) – an organic molecule comprising a perylene core and anhydride end groups, whose structure is shown in Figure 3.1. This molecule features prominently in studies of metal–molecule interfaces because its solid phase is an organic semiconductor and because it can form highly ordered layers on selected metals [67].

Figure 3.1a shows the eigenvalue spectra computed using LDA, GGA, and B3LYP, compared to the experimental ultraviolet photoelectron spectrum obtained from both the gas phase and the solid state [68]. Also shown is the spectrum obtained from many-body perturbation theory, in the GW approximation [69], based on LDA as a starting point for the perturbation. A detailed discussion of many-body perturbation theory is outside the scope of this article. For our purposes, its salient point is that (unlike in DFT), in many-body perturbation theory eigenvalues can carry exact meaning as ionization energies, albeit at the cost of a significantly larger computational effort. It is readily observed that the GW calculation agrees reasonably well with experiment. It is also clear that (after allowing for a rigid shift to fix the ionization potential value) that the B3LYP calculation mimics the GW spectrum remarkably well (at a fraction of the computational cost). However, the LDA and GGA eigenvalue spectra do not mimic the GW result or experiment at all. In particular, they exhibit a spurious peak right in the plateau region of the experimental gas phase result.

This failure of LDA can be traced back to a problem that is easy to explain but difficult to systematically fix – the self-interaction error [30]. In the potential terms of

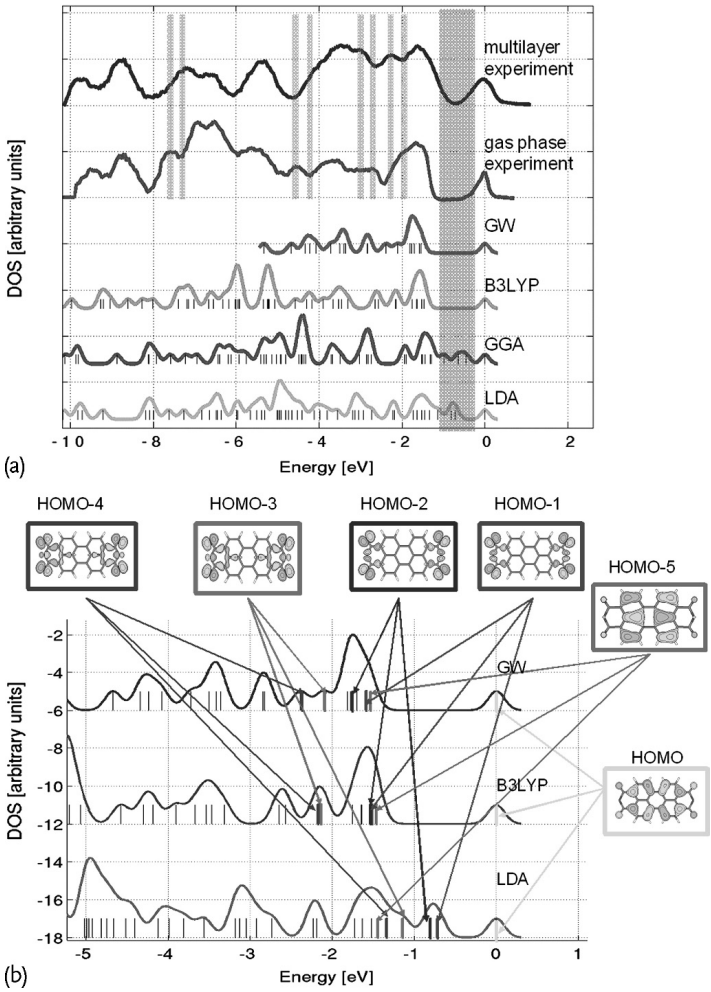

Figure 3.1 (a) Gas phase and multilayer experimental photoelectron spectrum of PTCDA, compared with GW, B3LYP, GGA, and LDA theoretical valence density of state curves for the PTCDA molecule. Light gray bars denote spectral features for which the gas phase and multilayer data differ appreciably. The dark gray bar denotes the HOMO–HOMO-1 gap, which differs significantly between the two experiments and also between different flavors of theory. (b) Top view of spatial distribution of orbitals associated with selected energy levels of PTCDA, as assigned by GW, B3LYP, and LDA calculations. Colors (shades) represent positive and negative parts of the orbital. The orbital numbering shown is the LDA one, with arrows pointing to the position of the same orbital in the different spectra. After Dori *et al.* [68]. Used with permission.

Eq. (3.1), we have, somewhat arbitrarily, selected to partition the consequences of electron–electron interaction to a Hartree part and an "everything else" exchange–correlation part. The Hartree term is an essentially classical expression that views the quantum charge probability distribution as a classical distribution of charges.

This, however, means that it is inherently in error, because each electron is repelled from the total charge in the system, including a spurious repulsion from *itself*. This is the self-interaction error. The spurious repulsion is particularly easy to see in one-electron systems, where clearly there should be no electron–electron repulsion at all, and yet the Hartree term is not zero. Because electron–electron interaction is, in principle, handled exactly in DFT, whatever error we are making in the Hartree term must be completely canceled out by the exchange–correlation term. Unfortunately, complete error cancelation is guaranteed for the exact exchange–correlation functional, but only partial cancelation is obtained in either L(S)DA or GGA.

The relation between the self-interaction error and the failure of LDA/GGA for PTCDA is made clear by a detailed orbital analysis, shown in Figure 3.1b [68]. It demonstrates that Kohn–Sham orbitals delocalized over the perylene core (e.g., "HOMO" and "HOMO-5" in the figure) yield LDA energies that are very close to the GW ones, that is, in agreement with experiment. However, Kohn–Sham orbitals localized on the anhydride groups (e.g., "HOMO-1" through "HOMO-4" in the figure) yield LDA energies that are significantly (well over an electron Volt) too high, resulting in a distorted spectrum. This is a clear self-interaction effect. For localized orbitals, the spurious self-interaction destabilizes the orbital and diminishes its binding energy. For delocalized orbitals, the self-interaction is much smaller because, at each point in space, the spurious same-electron contribution to the Coulomb potential comes from a greater average distance. For pedagogical reasons, we limit ourselves here to this qualitative argument. However, the self-interaction error can be quantified, showing unequivocally that it is indeed the self-interaction error that is driving this error [70]. Complete elimination of the self-interaction error would require full exact exchange, whereas B3LYP (and other standard hybrid functionals) only contains a fraction of exact exchange. Nevertheless, the mitigation of the self-interaction error, coupled with the nonlocal potential which partly mimics the "self-energy" nonlocal operator that is used in GW calculations [36], suffices to restore the predictive power of the DFT calculation.

A similar, but perhaps more nuanced, picture emerges by considering another prototypical organic electronics molecule – Cu phthalocyanine (CuPc). Figure 3.2 shows simulated density of states curves, obtained with PBE, PBEh, and GW using both the PBE and the PBEh results as a starting point for the perturbation (denoted by GW@PBE and GW@PBEh, respectively) [71]. In Figure 3.2a, both filled and empty states are compared to gas phase photoemission data and to two different thin film inverse photoemission data, respectively (comparison to additional experiments yields similar results). The calculated spectra were obtained from computed single-particle energy levels, broadened by convolution with a 0.35 eV wide Gaussian, in order to simulate the experimental broadening. In Figure 3.2b, filled state spectra, convoluted with a 0.15 eV wide Gaussian, are compared to higher-resolution gas phase data.

We first focus on the position of the HOMO-1 peak, because it affects the spectral shape noticeably and because lessons learned from it are directly applicable to other spectral features. Figure 3.2 illustrates the positions of the a_{1u} and $b_{1g\uparrow}$ orbitals. Similarly to the case of localized orbitals in PTCDA, with PBE the $b_{1g\uparrow}$ or-

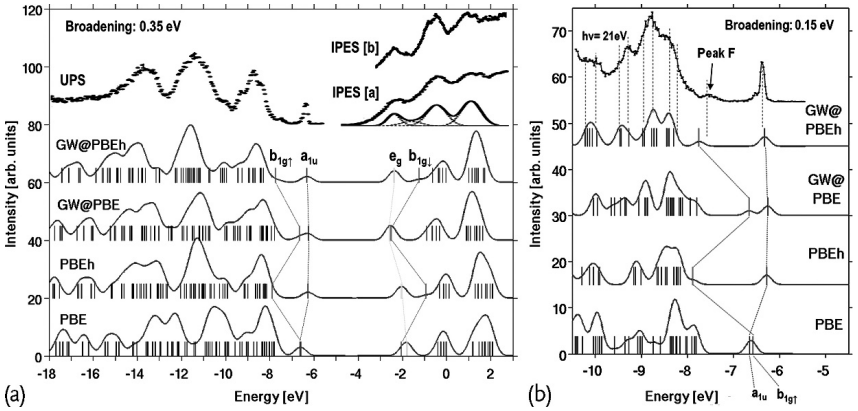

Figure 3.2 (a) Calculated DFT and GW spectra, obtained from computed energy levels (shown as sticks) by broadening via convolution with a 0.35 eV wide Gaussian, compared to gas phase UPS of Evangelista *et al.* [72] and to thin film IPES data of Murdey *et al.* [73] (shown with curve fitting results) and of Hill *et al.* [74] DFT spectra were shifted so as to align the HOMO and LUMO levels with computed ionization potential and electron affinity values. Experimental IPES spectra were shifted so as to align the LUMO peak with the computed GW@PBEh LUMO peak. (b) Same as (a) for filled states only, convoluted with a 0.15 eV wide Gaussian, compared to the higher-resolution gas phase UPS of Evangelista *et al.* After Marom *et al.* [71]. Used with permission.

bital, which is highly localized around the Cu atom, exhibits a large self-interaction error (as compared to the a_{1u} orbital, which is delocalized over the organic macrocycle). Therefore, it is shifted to a higher energy. This shift causes PBE to predict an incorrect ordering of the frontier orbitals, erroneously predicting the $b_{1g\uparrow}$ orbital to be the HOMO. Again as in PTCDA, this error is strongly reduced with a hybrid functional. In the PBEh spectrum. the correct ordering is restored and the overall agreement with experiment is much improved.

Complementary problems emerge in comparison to the inverse photoemission spectra shown in Figure 3.2. Empty states do not contribute to the Hartree term and therefore are not susceptible to self-interaction errors as such. However, because the SIE shifts the occupied $b_{1g\uparrow}$ orbital to a higher energy, it also shifts its empty counterpart, $b_{1g\downarrow}$, to a lower energy, with the overall spin-split energy severely underestimated. Thus, PBE also incorrectly predicting the $b_{1g\downarrow}$ orbital to be the LUMO, placing it $\sim$ 0.25 eV below the non-spin-split e_g orbital. Just as for the filled states, the correct ordering is restored by PBEh.

As expected, the GW@PBE spectrum is a significant improvement over the PBE one. However, unlike the case of PTCDA, detailed inspection shows that its accuracy is not sufficient, and that it "inherits" some of the errors of its starting point. For example, in the GW@PBE spectrum the $b_{1g\uparrow}$ orbital is almost degenerate with the e_g LUMO. In contrast, the GW@PBEh calculation maintains the PBEh orbital ordering, with a similar energy difference between the $b_{1g\uparrow}$ and e_g orbitals. With respect to PBEh, GW@PBEh brings both the $b_{1g\uparrow}$ and the $b_{1g\downarrow}$ related peaks even closer to their experimental value ("peak F" for the filled states [72], and a weak

peak identified via curve fitting for the empty states [73]). On the one hand, this shows that PBEh still has some quantitative limitations. On the other hand, it indicates yet again that PBEh is significantly superior to PBE, also as a starting point for high-accuracy GW calculations.

Unfortunately, the significant improvement in the electronic structure of molecules that is afforded by making the transition to a hybrid is accompanied by loss of accuracy for metals. For example, the width of the valence band of bulk sodium is already overestimated by PBE (3.3 eV versus an experimental value of 2.6 eV). But this overestimate gets to be markedly worse for PBEh, with a bandwidth of 4.3 eV [75]. Similar trends of diminished performance arise, for example, for the magnetic moment and exchange splitting of itinerant magnetic metals such as iron [75].

While, as yet, there is no complete solution for the need to balance performance across both sides of the metal–molecule interface, short-range hybrid functionals such as HSE appear to be a practical and reasonable compromise. On the organic side, HSE has been shown to mitigate self-interaction errors of the type shown in Figures 3.1 and 3.2 [76, 77]. This is reasonable: recall that HSE differs from conventional hybrid functionals in the absence of long-range exchange. However, the highly localized orbitals that are the most susceptible to self-interaction error are precisely the ones least affected by long-range contributions. On the metal side, using HSE results in deterioration in accuracy of the same kind mentioned above. However, the magnitude is smaller. For example, with HSE the valence bandwidth of Na is 3.7 eV [75]. This value is between those of PBE and PBEh. Again, this is reasonable, because in terms of its physical ingredients HSE is indeed "between PBE and PBEh." Another advantage of short-range hybrid functionals over conventional hybrid ones, which is not to be underestimated, is that they are much easier to apply to periodic systems in general and metallic ones in particular [45]. This is because Fock exchange is a slowly decaying long-range quantity, making its converged evaluation in a periodic system difficult. However, it is precisely these long-range difficulties which are avoided in a short-range hybrid.

While HSE is a useful "compromise functional" for many properties of the metal–molecule interface, one important issue it does not resolve is the level alignment problem, which remains open within DFT. This is demonstrated in Figure 3.3, which compares the fundamental gap of the benzene molecule, in the gas phase and graphite-physisorbed, as computed by PBE, HSE, and GW [78]. It is clear that both PBE and HSE make two different errors. First, their gas phase HOMO-LUMO gap is significantly too small with respect to that of GW. Second, they fail to predict the gap reduction upon physisorption. The first failure is due to an underestimate of the ionization potential and an overestimate of the electron affinity. As hinted above, this failure is due to the absence of long-range exchange. Indeed, it has been recently shown that range-separated hybrid functionals with long-range exact exchange ($b = 1$ in Eq. (3.9)) can yield quantitatively excellent predictions for the ionization potential and electron affinity in a wide variety of finite-sized systems, including benzene [79–81]. Unfortunately, such functionals are not yet suitable for handling the metallic side of the junction. The second

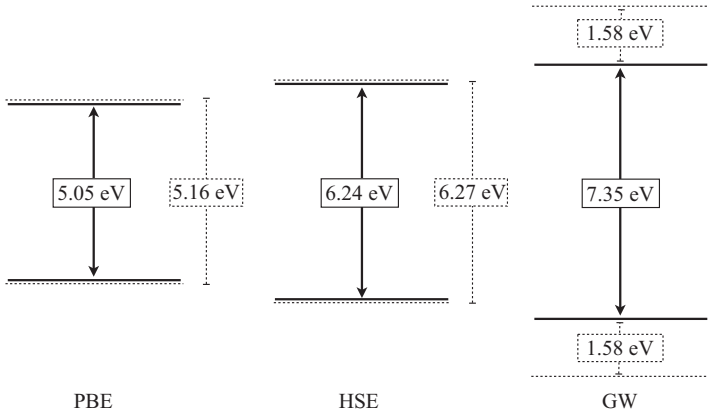

Figure 3.3 The fundamental gap of a benzene molecule, as computed from eigenvalue differences within PBE, HSE, and GW, for the gas phase (dashed lines) and graphite-physisorbed (solid lines) molecule. After Biller *et al.* [78]. Used with permission.

failure has to do with correlation. The physical mechanism for the gap reduction is that the removal or insertion of an electron from the molecule induces a polarization response in the metal [19]. This results in a net energy gain, which decreases the ionization potential and increases the electron affinity. From the DFT point of view, this is a nonlocal correlation effect, as it involves the *dynamic* response of the electron density in the metal to changes in the electron density of the molecule. As mentioned above in the context of van der Waals interactions, such correlation is lacking in conventional semilocal or hybrid functionals.

Here, it is very important to emphasize that the level alignment problem most certainly does not imply that DFT cannot be applied successful to molecule–metal interfaces. In fact, several studies have shown that even though the level alignment is incorrect, quantities deduced directly from the density distribution (in particular the interface dipole that is discussed extensively below) can still be in excellent quantitative agreement with experiment, even with a simple GGA approach [82–84]. Hence, one should carefully consider the suitability of each choice of functional for the task at hand.

To summarize this section, we hope to have convinced the reader, through illustrative examples, that it is important to keep in mind the various strengths and weaknesses of various DFT-based approaches in order to perform a meaningful analysis of the metal–molecule interface.

3.4
Understanding Metal–Molecule Interface Dipoles from First Principles

A central question in the study of metal–molecule interfaces, and indeed organic–inorganic interfaces in general, is that of the interface dipole [85]. An interface

dipole will affect level alignment and transport across the organic/inorganic junction and is therefore important technologically. It is also of interest from a basic science point of view, because a host of nontrivial mechanisms, discussed below, can control it.

The detailed mechanisms at work depend on the nature of the metal–molecule contact. Generally one distinguishes between three different types of systems – physisorbed, weakly chemisorbed, and strongly chemisorbed, depending on the chemistry controlling the metal–molecule interaction.

The first category consists of inert gas atoms and molecules such as *n*-alkanes, that adsorb on metal surfaces without forming chemical bonds between adsorbates and substrates. Even though these atoms and molecules do not possess a permanent dipole in the gas phase, in their physisorbed state sizable interface dipoles are observed. Two origins for this phenomenon have been proposed [85–87]. The first one is the so-called image force effect [86]. When inert gas atoms or molecules are located in proximity to a metal surface, electrons of those atoms or molecules are attracted towards the metal substrate by their image charges induced in the metal surface, producing polarization of the adsorbates. The second mechanism originates from the Pauli repulsion [87]. At a metal surface, electrons of the metal substrate penetrate into the vacuum region. When closed shell atoms or molecules approach the metal surface, penetrating electrons are pushed back to the substrate by the Pauli repulsive interaction with electrons of adsorbed molecules. Bagus *et al.* pointed out that electrons move from atoms with more localized orbitals to those with more delocalized orbitals [87]. In both cases, the closed shell adsorbate becomes slightly positive and the metal substrate becomes slightly negative, lowering the metal work functions.

Because in physisorbed systems the interaction between adsorbate and substrate is small, it is expected that the interface is close to ideal also for transport purposes, namely, that the ideal Schottky limit of metal–semiconductor interfaces [88] is approached. This can be quantified by the interface slope parameter S defined by

$$S = \frac{d\Phi_B^n}{d\Phi_m} = 1 + \frac{d\Delta}{d\Phi_m} \tag{3.10}$$

where Φ_m, Φ_B^n, and Δ are the substrate work function, the electron injection barrier, and the interface dipole, respectively. For the ideal Schottky limit, S=1.

For weakly chemisorbed systems, Flores *et al.* proposed a simple model based on the concept of an induced density of interface states (IDIS) [89–93]. This model assumes that the chemical interaction between the organic molecules and the metal creates an IDIS in the organic energy gap. Although the chemical interaction is weak, this IDIS is large enough to define the charge neutrality level (CNL) of the adsorbed organic molecule, E_{CNL}, which controls the extent of the charge transfer between organic molecules and metal surfaces. Figure 3.4a,b shows energy band diagrams at organic/metal interfaces before and after contact. The amount of charge transferred from the adsorbate to the metal substrate can be expressed by

$$\Delta N^A = (\Phi_m + \Delta - E_{CNL}) \times D(E_F) \tag{3.11}$$

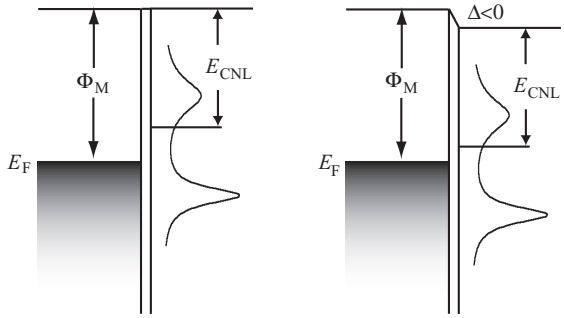

Figure 3.4 Energy diagram for organic/metal interfaces (a) before charge transfer, and (b) after charge transfer. The induced density of interface states (IDIS) is shown.

where $D(E_F)$ is the density of the IDIS at the Fermi level (E_F). The interface dipole is assumed to originate primarily from this charge transfer and can be calculated from

$$\Delta = -\frac{Z_C}{\epsilon_i A}(\Phi_m + \Delta - E_{CNL}) \times D(E_F) \tag{3.12}$$

where A is the surface area covered by one molecule and ϵ_i is the permittivity of the interfacial layer, which is assumed to be close to that of vacuum, ϵ_0. Substituting Eq. (3.12) in Eq. (3.10), we obtain

$$S = \frac{1}{1 + \frac{Z_C D(E_F)}{\epsilon_0 A}} \tag{3.13}$$

Although this model is quite simple, it provides an intuitive explanation of energy level alignment at weakly interacting organic/metal and organic/organic interfaces and its authors concluded that it provides for a predictive description of the energy level at various organic/metal interfaces.

For strongly chemisorbed systems, there is broad consensus that the overall interface dipole is approximately given by a sum of the bond dipole and any molecular dipole, typically coming from an intrinsically polar head group [14, 15]. Importantly, these dipoles are typically partially depolarized by the electric field induced by other dipoles. The magnitude of depolarization is strongly dependent on the backbone polarizability [14, 15].

Following this brief survey, we now present some recent studies that show how DFT allows us to examine the accuracy and applicability of these simple models and ultimately to gain further insight into the interface dipole. We focus primarily on physisorbed and weakly chemisorbed systems, as dipolar phenomena in strongly adsorbed systems have been reviewed in detail elsewhere [14, 15] (but one example of collective dipolar phenomena in strongly chemisorbed systems is given in Section 3.5).

3.4.1
n-Alkane/Metal Interfaces

Because *n*-alkane/metal interfaces are typical physisorbed systems, the interface slope parameter, S, is expected from the simple model presented above to be close to 1. However, it was reported to be $S \simeq 0.6$ [85]. To understand the origin for the dependence of the interface dipole on metal substrates, Morikawa *et al.* carried out first-principles theoretical calculations based on DFT [94]. Figure 3.5 shows the atomic geometry of a *n*-butane/metal interface, and Figure 3.6 shows interface dipoles induced by the adsorption of *n*-alkane molecules on various metal surfaces as a function of the molecule–metal distance (Z_C).

The interface dipole is estimated by calculating the work function change induced by adsorption of a monolayer on the metal substrate, because the majority

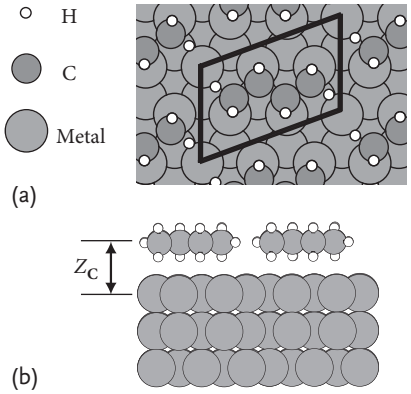

Figure 3.5 (a) Top view and (b) side view of a *n*-butane/metal interface. After Morikawa *et al.* [94], used with permission.

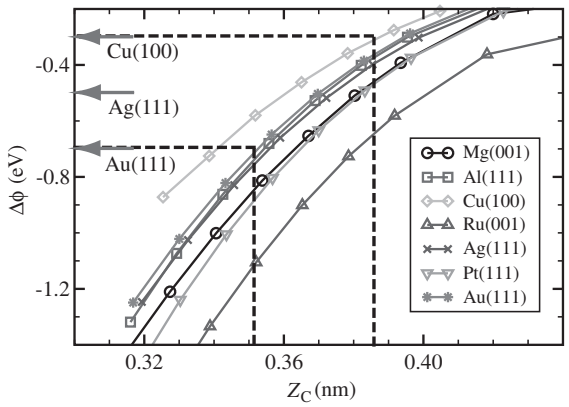

Figure 3.6 Interface dipoles as function of molecule–metal distance (Z_C) for *n*-alkane/metal interfaces. After Morikawa *et al.* [94], used with permission.

of the interface dipole is induced at the very interface, between the metal substrate and the first molecular layer. Two important conclusions can be drawn from Figure 3.6. One is that if molecules are fixed at the same Z_C on various metals, the induced interfacial dipole moments are quite similar, except Ru(001). For example, the work functions of Cu(100), Au(111), and Pt(111) are 4.59 eV, 5.31 eV, and 5.70 eV, respectively, and the difference is more than 1 eV. On the other hand, if *n*-alkane molecules are located at $Z_C = 0.38$ nm from the substrate, the induced dipoles are in the range 0.4–0.6 eV for all the three substrates. This means that if the adsorption geometries are the same for various *n*-alkane/metal interfaces, S would be about 0.8 and the interface would be closer to the Schottky limit, in agreement with the intuitive understanding. However, the experimentally observed interface slope parameter is $S \simeq 0.6$ as mentioned above, and the work function changes induced by adsorption of *n*-alkane molecules on Cu(100) and Au(111) are 0.3 and 0.7 eV, respectively. The other important conclusion drawn from Figure 3.6, then, is that the experimentally observed substrate dependence of the interface dipole comes mainly from the difference in interface geometries, especially the molecule–metal distance Z_C.

3.4.2 Benzene/Metal Interfaces

Benzene/metal interfaces are prototypical systems of interfaces between functional aromatic compounds and metal electrodes. Accordingly, benzene on metal surfaces has been extensively studied both experimentally and theoretically [95–110]. Bilić *et al.* [104] studied benzene on noble metal surfaces using DFT and showed that their calculations reproduce major qualitative features of the experimental results. However, the magnitude of the binding energy was severely underestimated due to the lack of the long-range van der Waals interactions [104]. Bagus *et al.* theoretically studied benzene on noble metal surfaces to compare computational results with experimental ones and showed successfully that the exchange effect is an important cause of the interface dipole layer [95–97]. They used second-order Møller–Plesset perturbation (MP2) method to reproduce the long-range vdW interactions, which limited their calculations to small clusters. Moreover, the MP2 method tends to overestimate the van der Waals (vdW) interactions, creating a need for more accurate methods [111, 112]. Toyoda *et al.* have investigated benzene adsorbed on Cu(111), Ag(111), and Au(111) surfaces by using DFT with van der Waals corrections [113, 114]. Figure 3.7a,b shows the calculation model for benzene adsorbed on noble metal surfaces, with a (3×3) surface unit cell.

The adsorption energy E_{ad} is defined by

$$E_{ad} = E(\text{adsorbate/metal}) - E(\text{adsorbate}) - E(\text{metal}) \tag{3.14}$$

where E(adsorbate/metal), E(adsorbate), E(metal) are the total energies of the adsorbed system, the isolated molecule, and the clean metal surface, respectively. A negative value of E_{ad} means that the adsorbed system is energetically favorable relative to the isolated state. To estimate the adsorption energies, Toyoda *et al.* employed

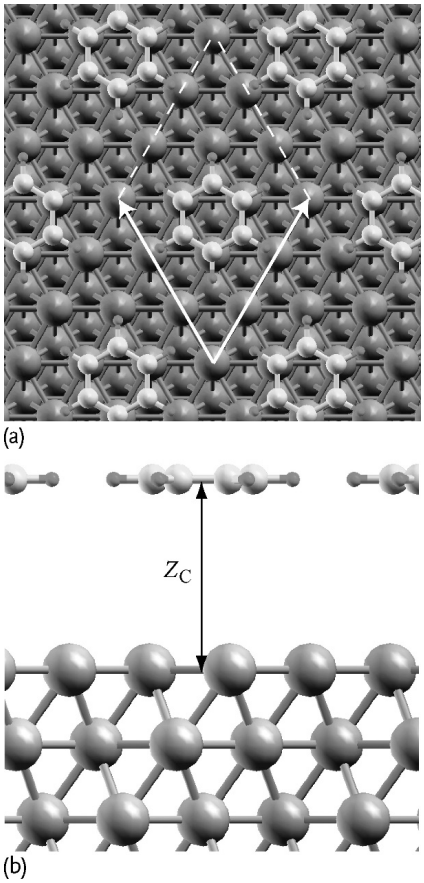

Figure 3.7 (a) Top view and (b) side view of a benzene/metal interface. After Toyoda *et al.* [114], used with permission.

not only a GGA calculation but also two of the van der Waals methods mentioned in Section 3.2: Grimme's semiempirical pairwise corrections [57, 58] (DFT-D) and the Dion *et al.* van der Waals functional [53] (vdW-DF). Table 3.1 summarizes the equilibrium distances (Z_C^{GGA}, $Z_C^{DFT\text{-}D}$, and Z_C^{vdW}) and the adsorption energies (E_{ad}^{GGA}, $E_{ad}^{DFT\text{-}D}$, and E_{ad}^{vdW}) calculated by GGA, DFT-D, and vdW-DF, respectively. The E_{ad}^{vdW} values agree well with the experimental values, and this agreement is even better than those of the MP2 method [95, 96]. $E_{ad}^{DFT\text{-}D}$ for Cu agrees well with the experimental value, whereas for Ag and Au, the absolute values are overestimated by ~ 0.2 eV. This is likely partly because the C_6 coefficients for heavier atoms are overestimated by Grimme's scheme [115] and partly due to the absence of screening of the substrate electrons in the determination of the pairwise coefficients, going effectively beyond the pairwise description [60], a point we return to below for PTCDA. On the other hand, the E_{ad}^{GGA} values are an order of magnitude smaller

Table 3.1 The equilibrium distances (Z_C^{GGA}, $Z_C^{DFT\text{-}D}$, and Z_C^{vdW}), and the adsorption energies (E_{ad}^{GGA}, $E_{ad}^{DFT\text{-}D}$, and E_{ad}^{vdW}) calculated by GGA, DFT-D, and vdW-DF, respectively, along with the equilibrium distances and the adsorption energies calculated by MP2, and the experimentally determined adsorption energies for benzene on Cu(111), Ag(111), and Au(111).

	Surface	Cu(111)	Ag(111)	Au(111)
GGA	Z_C^{GGA}/nm	0.37	0.37	0.37
	E_{ad}^{GGA}/eV	–0.050	–0.061	–0.068
DFT-D	$Z_C^{DFT\text{-}D}$ / nm	0.29	0.29	0.31
	$E_{ad}^{DFT\text{-}D}$/eV	–0.56	–0.64	–0.79
vdW-DF	Z_C^{vdW} / nm	0.37	0.37	0.37
	E_{ad}^{vdW}/eV	–0.55	–0.49	–0.55
MP2	Z_C/nm	0.36 [a]	0.37 [b]	0.38 [c]
	E_{ad}/eV	–0.35 [a]	–0.33 [b]	–0.31 [b]
Exp.	E_{ad}^{exp}/eV	–0.58 [d]	–0.42 [e]	–0.60 [f]

[a] [96]
[b] [95]
[c] [95, 97]
[d] [96, 98]
[e] [95, 99]
[f] [95, 100]

than the experimental values, in agreement with previous GGA results [104]. This indicates that the interaction between benzene and close-packed noble metal surfaces is predominantly due to the dispersion interaction, confirming that it should be classified within the physisorbed systems.

Although the E_{ad} values significantly depend on the choice of the energy functionals, the Z_C^{GGA} and Z_C^{vdW} values are the same. Moreover, the Z_C values calculated by MP2 are also almost the same. On the other hand, the $Z_C^{DFT\text{-}D}$ values are smaller than those calculated by the other methods. Romaner *et al.* reported that for PTCDA on noble metal surfaces, Z_C^{vdW}s are systematically overestimated [116]. Because the benzene–substrate distances have never been measured experimentally, it is not possible to compare the calculated results with experimental ones. However, as discussed below, by comparing the calculated vacuum level shifts with the experimental ones, we can indirectly deduce the most probable benzene-metal distance and conclude that the DFT-D method provide a reasonable benzene-metal distance while the GGA and the vdW-DF methods overestimate it.

The interface dipole $\Delta\phi'$ is calculated by

$$\Delta\phi' = \phi\,(\text{adsorbate/metal}) - \phi\,(\text{metal}) \tag{3.15}$$

where ϕ(adsorbate/metal) and ϕ(metal) are the work function of the adsorbed system and the clean metal surface, respectively. To estimate the work function change

the experimental surface molecular density of the adsorbate on the surface, n_{metal}, is used. A coverage-corrected $\Delta\phi'$ is obtained, assuming that depolarization effects [14, 15] can be neglected, by using a simplified form of the Helmholtz equation [117]:

$$\Delta\phi = \Delta\phi' \frac{n_{\mathrm{metal}}}{n_0} \tag{3.16}$$

where $\Delta\phi$ is the corrected work function change, and $n_0 \equiv A_0^{-1}$, where A_0 is the area of the surface unit cell of the adsorbed systems.

Table 3.2 summarizes $\Delta\phi$s calculated by GGA at several distances. The calculated $\Delta\phi$s at $Z_{\mathrm{C}}^{\mathrm{DFT\text{-}D}}$ are in excellent agreement with the experimental values of −1.05 [97], −0.70 [95], and −1.10 eV [97], for Cu, Ag, and Au, respectively. On the other hand, the absolute values of the calculated $\Delta\phi$s at $Z_{\mathrm{C}}^{\mathrm{GGA}}$ and $Z_{\mathrm{C}}^{\mathrm{vdW}}$ are significantly underestimated, which comes from the overestimation of the $Z_{\mathrm{C}}^{\mathrm{GGA}}$ and $Z_{\mathrm{C}}^{\mathrm{vdW}}$.

To single out the electronic factor contributing to the formation of the interface dipole, Toyoda *et al*. investigated the interface dipole using the same benzene coverage for the three metal surfaces, as shown in Figure 3.8. The substrate dependence of $\Delta\phi$ on Z_{C} is almost the same for the three metal surfaces, indicating that the interface is in the Schottky limit. This is consistent with previous results in which the exchange effect was an important cause of the interface dipole formation at benzene/metal interfaces [95–97]. Experimentally, however, the substrate dependence of the interface dipole on the work function behavior is as close to the nonideal (Bardeen) limit ($S = 0$), then to the ideal $S = 1$ Schottky limit, with $S \sim 0.46$. As before, this clearly shows that the substrate dependence of the interface dipole comes from geometric factors such as benzene–substrate distance and surface-molecular density, rather than from stronger benzene–substrate interaction.

Table 3.2 Work function changes ($\Delta\phi$) calculated by GGA at $Z_{\mathrm{C}}^{\mathrm{GGA}}$, $Z_{\mathrm{C}}^{\mathrm{DFT\text{-}D}}$, and $Z_{\mathrm{C}}^{\mathrm{vdW}}$, along with the experimental work function change ($\Delta\phi^{\mathrm{exp}}$) for benzene on Cu(111), Ag(111), and Au(111).

Surface	GGA Z_{C}/nm	$\Delta\phi$/eV	MP2 $\Delta\phi$/eV	Exp. $\Delta\phi^{\mathrm{exp}}$/V
Cu(111)	$Z_{\mathrm{C}}^{\mathrm{DFT\text{-}D}} = 0.29$	–1.09	–1.08 [a]	–1.05 [a]
	$Z_{\mathrm{C}}^{\mathrm{GGA}}$, $Z_{\mathrm{C}}^{\mathrm{vdW}} = 0.37$	–0.33	–	–
Ag(111)	$Z_{\mathrm{C}}^{\mathrm{DFT\text{-}D}} = 0.29$	–0.71	–0.77 [b]	–0.70 [c]
	$Z_{\mathrm{C}}^{\mathrm{GGA}}$, $Z_{\mathrm{C}}^{\mathrm{vdW}} = 0.37$	–0.25	–	–
Au(111)	$Z_{\mathrm{C}}^{\mathrm{DFT\text{-}D}} = 0.31$	–1.06	–0.87 [a]	–1.10 [a]
	$Z_{\mathrm{C}}^{\mathrm{GGA}}$, $Z_{\mathrm{C}}^{\mathrm{vdW}} = 0.37$	–0.48	–	–

[a] [97]
[b] [95]
[c] [99]

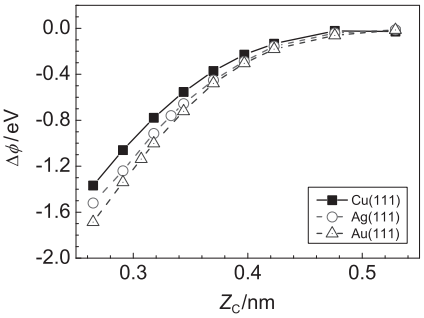

Figure 3.8 Work function change ($\Delta\phi$) as a function of Z_C for benzene on Cu(111), Ag(111), and Au(111) provided that the surface molecular densities on the three metal surfaces are assumed to be the same. After Toyoda *et al.* [114], used with permission.

3.4.3
Pentacene/Metal Interfaces

Pentacene ($C_{22}H_{14}$) is one of the most typical compounds for organic field effect transistors and the interface between pentacene and metal surfaces has been studied extensively both experimentally and theoretically [118–131]. Toyoda and coworkers investigated the atomic geometries and electronic properties of pentacene/metal interfaces in detail using DFT [129–131]. Figure 3.9a shows the adsorption geometry of pentacene on an FCC(111) surface, and Figure 3.9b shows the adsorption energy of pentacene on the Cu(111) surface. As seen in Figure 3.9b, again the potential energy curve calculated by GGA has a shallow minimum, whereas those by DFT-D and vdW-DF have deeper minima. The equilibrium distance calculated by DFT-D is smaller than those calculated by GGA and vdW-DF. The adsorption energies calculated by DFT-D and vdW-DF agree quite well with the experimental value of −1.6 eV. The calculated Z_C by DFT-D (0.24 nm) is in excellent agreement with the experimental value of 0.234 nm [124]. On the other hand, the calculated Z_C by GGA (0.42 nm) and by vdW-DF (0.37 nmx) are significantly overestimated by 0.13 $\sim$ 0.18 nm compared with the experiment. As is the case for benzene on noble metal surfaces, the calculated Z_Cs by vdW-DF are overestimated, possibly because of the exchange part of the specific GGA used in vdW-DF being too repulsive. Thus, we again find that the DFT-D method gives reasonable molecule–metal distance while the GGA and the vdW-DF methods overestimate it.

Figure 3.9c shows $\Delta\phi$s in pentacene adsorbed on Cu(111), Ag(111), and Au(111) surfaces as function of Z_C. The experimentally determined $\Delta\phi$s on Cu(111), Ag(111), and Au(111) are indicated by horizontal dashed lines, whereas the experimentally determined pentacene-Cu(111) distance and the equilibrium distances on Ag(111) and Au(111) calculated by DFT-D are shown by vertical dotted lines. The calculated $\Delta\phi$s at equilibrium Z_C agree well with the experimental values, while the absolute values of the calculated $\Delta\phi$s at equilibrium Z_Cs calculated by GGA or vdW-DF are significantly underestimated, which comes from the overes-

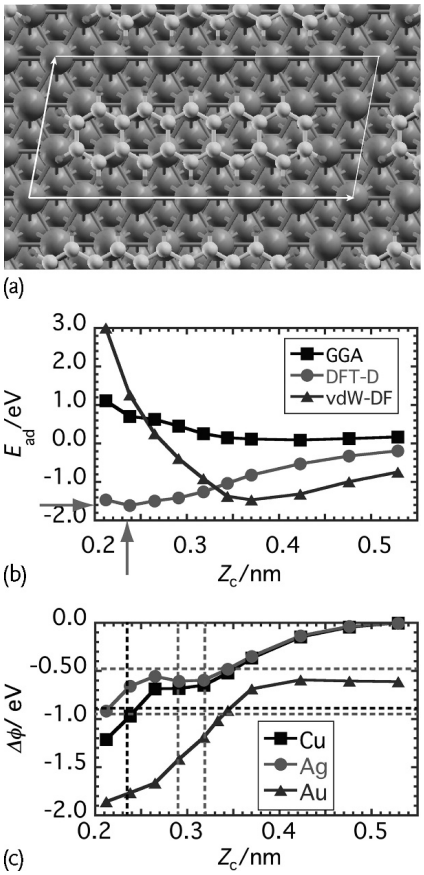

Figure 3.9 (a) Top view of pentacene adsorbed on an FCC(111) surface. (b) Adsorption energy of pentacene on Cu(111) as a function of pentacene-metal distance (Z_C). The experimentally observed pentacene-Cu(111) distance [124] and the adsorption energy [129] are shown by arrows. (c) Work function change induced by pentacene adsorption on Cu(111), Ag(111), and Au(111) surfaces. The equilibrium distances calculated by DFT-D are shown by vertical dotted lines. The experimental values of $\Delta\phi$ on Cu(111) [124], Ag(111) [118], and Au(111) [119, 132] are shown by horizontal dashed lines. Square, circle, and triangle lines are for Cu(111), Ag(111), and Au(111), respectively. After Toyoda *et al.* [131], used with permission.

timation of the Z_C as pointed out above. As seen in Figure 3.9c, the trends for Cu(111) and Ag(111) are quite similar to each other, whereas Au(111) is different. On Au(111) at large Z_C, $\Delta\phi$ converges to a negative value of −0.6 eV. This unreasonable behavior comes from an artificial electron transfer from pentacene to the substrate, owing to the unrealistic level alignment afforded by GGA. In reality, $\Delta\phi$ should converge to zero at large Z_C, coinciding with the results for the other two substrates. As Z_C decreases, $\Delta\phi$ decreases monotonically on Au(111), presumably because of the push back (Pauli repulsion) effect. In contrast, on Cu and Ag, $\Delta\phi$s

take a plateau-like shape at around 0.26 nm $< Z_C <$ 0.32 nm. The hybridization between the pentacene LUMO and the substrate states takes place at Z_C smaller than about 0.3 nm, and therefore the plateau comes from the counter-polarization due to the back donation from the substrate to the pentacene. Calculated results indicate that as the pentacene molecule approaches the substrate, S decreases from 1 to nearly 0. This result suggests a transition from the Schottky limit to the Bardeen limit, which is consistent with an intuitive explanation that the interface is in the Schottky limit if the pentacene–substrate interaction is weak whereas the interface is in the Bardeen limit if the interaction is strong. Experimentally, the slope parameter for pentacene on several substrates is evaluated to be ~ 0.5, which is an intermediate between the two limits. This suggests that this system should be treated as a weakly chemisorbed system. The slope trend is due to the different adsorption height on the different substrate, indicated by the DFT-D calculations. The slope parameter from $\Delta\phi$ at the adsorption distance is estimated from DFT-D to be ~ 0.15, which is underestimated compared to the experimental value of about 0.5. This might be due to the overestimation of the calculated $\Delta\phi$ on Au.

It is interesting to examine the validity of the simple IDIS model by comparing with DFT calculations. Toyoda *et al*. estimated the number of electrons transferred from the metal surface to adsorbed molecules (ΔN^A) and calculated the interface dipole using Eq. (3.12) [129]. Figure 3.10a shows ΔN^A as function of Z_C for pentacene on the Cu(111) surface, while Figure 3.10b shows the vacuum level shifts as a function of Z_C for pentacene on the Cu(111) surface. The vacuum level shift estimated by the IDIS model is denoted by Δ_{IDIS} and the work function change by using the self-consistent GGA results is denoted by $\Delta\phi$.

The ΔN^A curve exhibits a minimum at around $Z_C \sim 0.34$ nm. At large Z_C, holes are induced in the occupied states and Δ_{IDIS} is reduced, in agreement with the

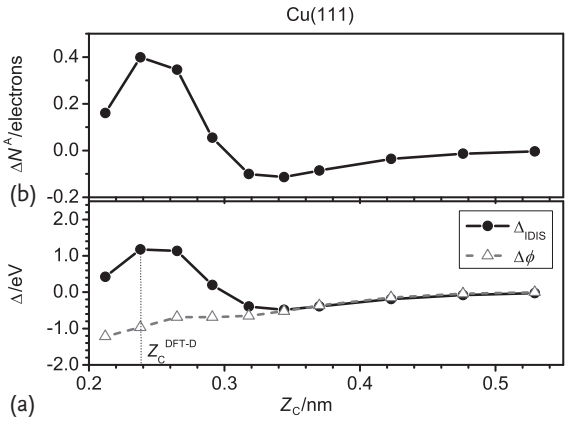

Figure 3.10 (a) Number of electrons transferred from the substrate to the adsorbate (ΔN^A) as a function of Z_C for pentacene on Cu(111). (b) Vacuum level shifts estimated by the IDIS model (Δ_{IDIS}) and the work function change ($\Delta\phi$) as a function of Z_C, with the position of $Z_C^{DFT\text{-}D}$ shown by a vertical dotted line. After Toyoda *et al.* [129], used with permission.

GGA results. As the molecule approaches the substrate, the unoccupied states are partially filled due to hybridization between molecular LUMO states and substrate states, and Δ_{IDIS} is increased. Accordingly, Δ_{IDIS} agrees fairly well with $\Delta\phi$ at large Z_{C}, whereas Δ_{IDIS} tends to deviate from $\Delta\phi$ at small Z_{C}, where back donation from the substrate to the adsorbate becomes large. Therefore, we conclude that as long as the system can be considered as a weakly adsorbed one, namely, an organic–metal distance larger than 0.3 nm in this case, the IDIS model is reasonably valid, but its validity degrades strongly as soon as stronger chemisorption sets in.

3.4.4 PTCDA/Metal Interfaces

We have already mentioned in Section 3.3 that in its solid, semiconducting phase PTCDA forms highly ordered layers on selected metals [67]. It is therefore no surprise that PTCDA adsorption on metal surfaces has been intensively studied as a prototypical molecule–metal interface [60, 89, 116, 133–142].

The combination of the aromatic core and the anhydride side groups suggests that the PTCDA/metal system can show some traits of both weakly chemisorbed and more strongly chemisrobed systems. Consequently, earlier DFT studies generated some controversy due to the above-discussed difficulty of treating weak van der Waals interaction between PTCDA and metal surfaces by using conventional GGA [136, 137, 143, 144]. More recent work showed that calculations with nonlocal correlation can reasonably reproduce the adsorption states of PTCDA on metal surfaces [116, 138]. The issue was fully resolved recently by Ruiz *et al.* [60]. They showed that by combining Tkatchenko–Scheffler pairwise corrections with the Lifshitz–Zaremba–Kohn theory for the nonlocal Coulomb screening within the bulk, quantitative agreement between theory and experiment for both the adsorption distance and the adsorption energy is obtained. Their comparison of a variety of DFT-based methods for this system is given in Figure 3.11.

Turning to the electronic structure, Romaner *et al.* circumvented the van der Waals problem by using GGA calculations based on the experimentally reported molecule–metal distances for studying PTCDA in its "herringbone" structure on the Ag(111), Cu(111), and Au(111) surfaces (see Figure 3.12) [116]. The resulting projected densities of states onto PTCDA molecular orbitals are shown in Figure 3.13. Clearly, if the experimentally reported molecule–metal distances are employed, agreement with experiment is quite reasonable. We note that the difficulties experienced by using GGA for gas phase PTCDA [68], highlighted in Figure 3.1, are strongly mitigated here due to interaction with the delocalized metal electrons. For the relatively short molecule–metal distances on Ag(111) and Cu(111) (2.86 and 2.66 Å, respectively), significant hybridization is found. In particular, the LUMO is partly occupied and about 0.5 electrons are estimated to be transferred from the metal substrate to the PTCDA. On the other hand, at the larger molecule–metal distance on Au(111) (3.27 Å), the hybridization is weaker and the LUMO remains just above the Fermi level.

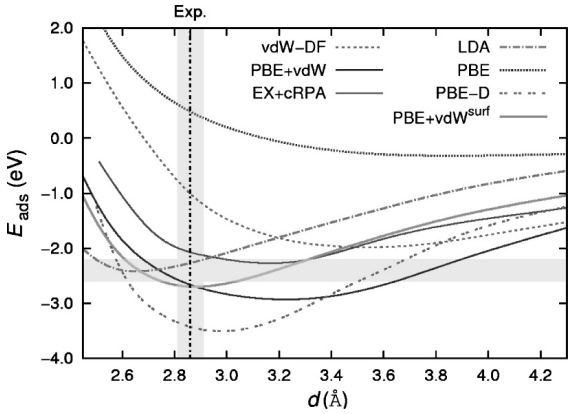

Figure 3.11 Adsorption energy E_{ads} as a function of vertical distance d, for PTCDA on Ag(111), employing different theoretical approaches as denoted in the figure. Experimental values, including their uncertainty, are indicated by shaded intervals. After Ruiz *et al.* [60], used with permission.

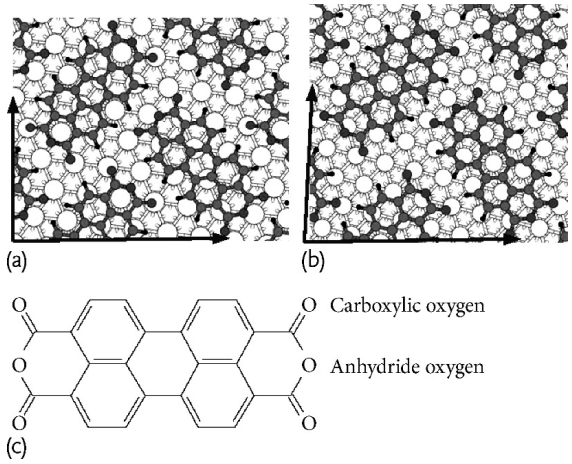

Figure 3.12 Top view of PTCDA adsorbed on Ag(111) (a) and on Cu(111) (b). Molecular structure of PTCDA (c). After Romaner *et al.* [116], used with permission.

The large charge transfer from the metal substrate to the PTCDA increases the work function by 0.24 eV on the Ag(111) substrate. On Cu(111), however, the work function is reduced by 0.29 eV despite this effect because of the larger Pauli repulsion ("push back") effect due to the shorter molecule–metal distance. On Au(111), charge transfer is much smaller and the work function is reduced by 0.34 eV. These calculated work function changes agree with experimental values reasonably well. Thus, PTCDA appears as a subtle case of chemisorption of varying strength, depending on substrate and adsorption geometry.

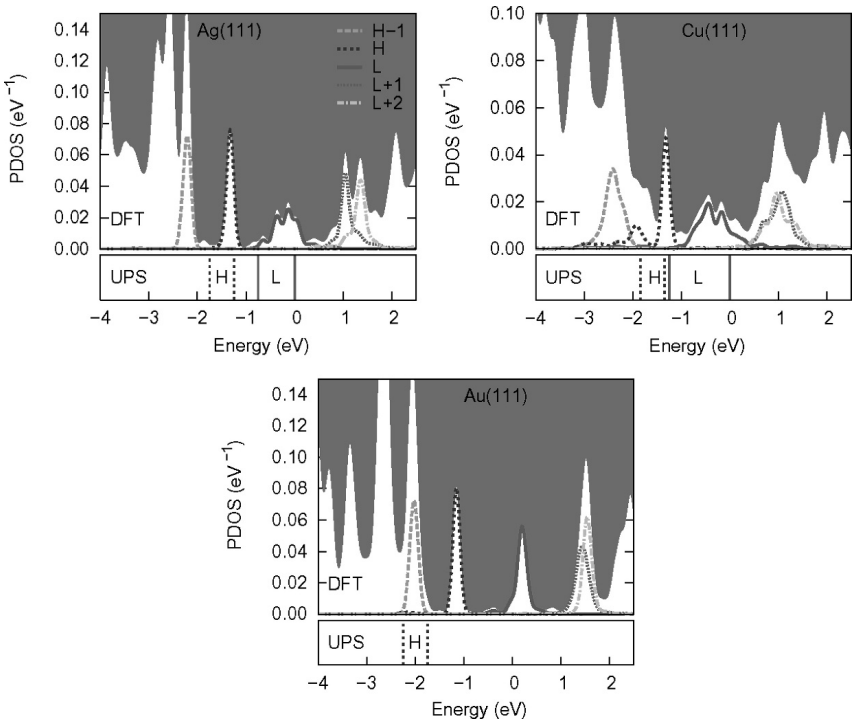

Figure 3.13 Projected density of states onto molecular orbitals for PTCDA on Ag(111), Cu(111), and Au(111) surfaces. The HOMO and LUMO peak positions observed by UPS are indicated at the bottom. After Romaner *et al.* [116], used with permission.

3.5
Two Examples of Collective Effects at Metal–Molecule Interfaces

In our introductory remarks, we have emphasized the emergence of highly nontrivial collective effects at metal–molecule interfaces. Furthermore, we partly motivated first principles calculations for such interfaces by the need to explain and ultimately predict collective effects that defy explanation by textbook models. Therefore, we devote the final section of this chapter to two different recent examples where DFT has played a prominent role in predicting collective effects.

3.5.1
Quantum-Confined Stark Effect in Monolayers of Molecules Consisting of Polar Repeating Units

A well-known collective effect in polar monolayers is that the dipolar array results in a nonvanishing electric field across the monolayer (see [14, 15], and references therein). Akin to a parallel-plate capacitor, this results in a potential drop across the monolayer, which is frequently used for work function modulation. These ideas

can be extended further by considering a monolayer comprised of repeating polar units, with recent theoretical work performed on oligopyrimidines as a model system [145–147].

Rissner *et al.* have identified, using DFT calculations with the HSE short-range hybrid functional, an interesting collective effect for a Au-adsorbed monolayer of terpyrimidinethiols [146]. For this system, a comparison of LDA, HSE, and explicitly self-interaction corrected calculations showed that use of HSE is essential to obtaining the correct ordering of close-lying σ and π states while retaining a realistic description of the metallic Au. They observed that in the transition from molecule to self-assembled monolayer, frontier states increasingly localize on opposite sides of the monolayer, as shown in Figure 3.14. The direction of localization is opposite for filled and empty orbitals, as well as for "up" and "down" monolayers (distinguished by the relative position of the nitrogen atoms in each ring with respect to the thiol group). Furthermore, this polarization is, in several instances, in the direction *opposite* to the polarization of the overall charge density.

This behavior was interpreted by Rissner *et al.* by analogy to inorganic semiconductor quantum wells, which, just like the terpyrimidinethiols of Figure 3.14, can be regarded as semiperiodic systems. There, similar observations made under the influence of a, typically external, electric field are known as the quantum-confined Stark effect [148]. Without any external perturbation, in oligopyrimidine SAMs one encounters an energy gradient that is generated by the dipole moments of the pyrimidine repeat units. It is particularly strong and results in a substantial electric field of 1.6×10^7 V/cm, which is easily observed in plots of the electrostatic potential across the monolayer. Thus, in this case the collective electric field not only affects the interface dipole and work function as in the previous section, but also strongly affects all frontier molecular orbitals, modulating, for example, the

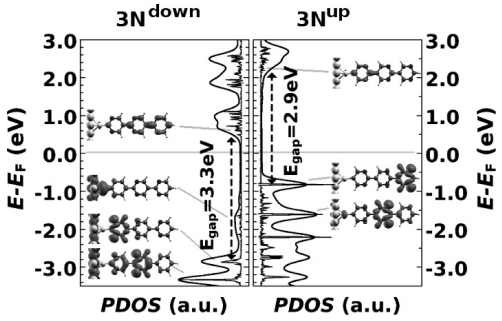

Figure 3.14 Partial density of states curves for a monolayer of terpyrimidinethiols on the ($\sqrt{3} \times \sqrt{3}$) Au(111) surface, for both "up" and "down" monolayers (distinguished by the relative position of the nitrogen atoms in each ring with respect to the thiol group). Only a small fraction of the metal atoms is shown. The Fermi energy is indicated as gray horizontal line. Curves are aligned at the average electrostatic energy across the monolayer. The thick black curves are Gaussian convolutions ($\sigma = 0.1$ eV) of the results of the calculation. Insets show band charge-densities of the frontier states and the band gap, as determined from the onsets of the respective nonbroadened DOS peaks, is indicated. After Rissner *et al.* [146], used with permission.

optical properties of the monolayer. These results explicitly show that when aiming to build a monolayer with a specific electronic structure, one may not only resort to the traditional technique of modifying the molecular structure of the constituents, but also try to exploit collective electronic effects.

3.5.2 Magnetic Molecule/Magnetic Metal Interfaces

In the previous example, the collective effects were due to long-range electrostatic effects and did not involve the explicit interaction between adsorbate and substrate. As a second, remarkable example we consider the electronic and magnetic properties emerging from the interaction of a magnetic molecule, Co-phthalocyanine (CoPc), with a magnetic metal, Fe [10]. Magnetic molecule/magnetic metal interfaces are important not only from the fundamental point of view, but also for possible applications in future organic spintronics devices.

Figure 3.15 shows the atomic geometry and electronic structure for a free CoPc molecule (Figure 3.15a) and for CoPc adsorbed on an Fe surface (Figure 3.15b), without and with vdW forces (Figure 3.15c,d) included during the relaxation. For the gas phase molecule, the energy ordering is adversely affected by the GGA calculation as in the CuPc example of Figure 3.2. Nevertheless, comparison with results from hybrid functionals [149] shows that the GGA calculation still correctly identifies the total molecular spin, S, as 1/2. As in previous examples, it is readily observed that both the atomic geometries and electronic structure of the Fe-adsorbed CoPc are strongly sensitive to vdW corrections. Without such corrections, the molecule–substrate distance is 3.1 Å and the molecule remains flat. With them, the molecule–metal distance is reduced to 2.6 Å and the molecule is no longer flat. Furthermore, hybridization between molecular orbitals and the substrate states is much stronger. By comparing simulated scanning tunneling microscopy (STM) images to experiment, as shown in Figure 3.16, it is shown that agreement between experimental and calculated STM images is excellent upon inclusion of vdW corrections. This also shows once more that GGA errors in the electronic structure are mitigated by hybridization with the delocalized metal electrons.

Importantly, the combination of a magnetic molecule and a magnetic substrate actually results in an adsorbed molecule with a net spin, S, of zero. This somewhat counter-intuitive result emerges due to the transfer of an electron from substrate to molecule. This does not mean, however, that all magnetic effects have been eliminated. Recall that spin-transport is not sensitive to the overall magnetization, but rather to the net magnetization of the current-carrying states, which can be completely different and even opposite [150]. Here, tunneling through the molecule exhibits a pronounced spin dependence due to spin-split molecule-surface hybrid states. This opens the door to *design* of the local spin-polarization and to selective spin injection [9].

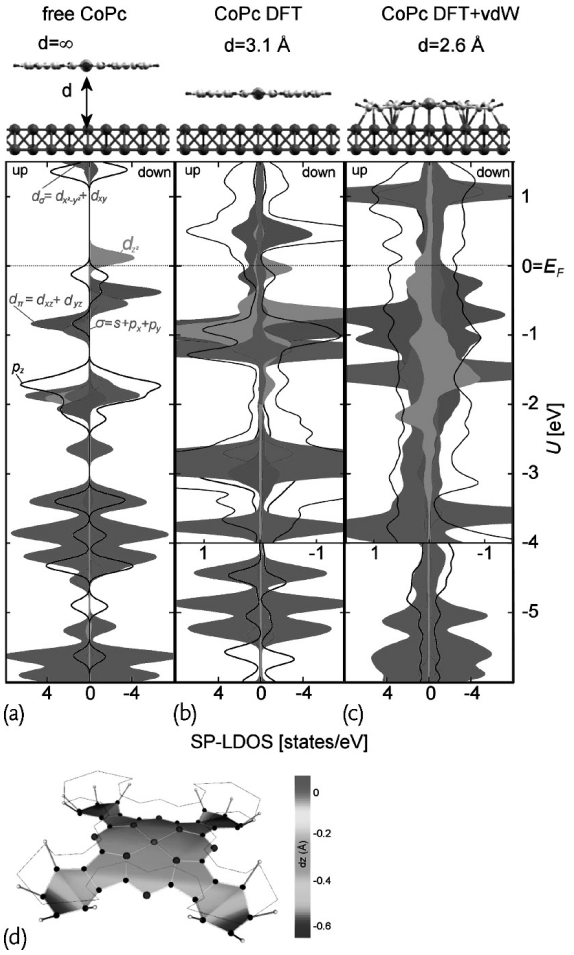

Figure 3.15 The atomic geometry and electronic structure for (a) a free CoPC, and (b) adsorbed on an Fe surface, (c) without and (d) with vdW forces included during the relaxation. After Brede *et al.* [10], used with permission.

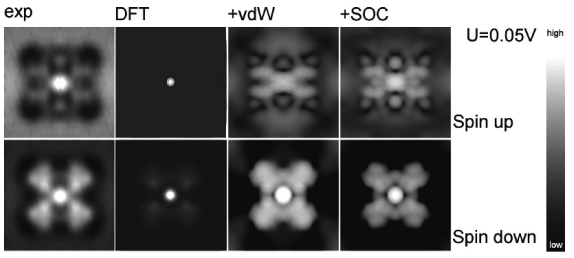

Figure 3.16 Comparison between experimental and simulated SP-STM images at $U = 0.05$ V. After Brede *et al.* [10], used with permission.

3.6 Concluding Remarks

In conclusion, in this chapter we have attempted to provide a short survey of insights into the behavior of metal–molecule interfaces obtained from first principles theory, with a strong emphasis on density functional theory. We have explained the underlying principles of the method and discussed challenges and recent progress in its successful application. We then surveyed how judicious application of the theory results in insights into the important problem of the interface dipole and how it allows for the identification and prediction of novel and often unexpected collective effects.

We end this chapter with two additional comments. On the methodological side, we discussed several instances where DFT calculations can go wrong and indeed we feel that, as in experimental work, one must be deeply familiar with the working of the methods employed in order to avoid artifacts. Nevertheless, we would like to stress that our message is not at all one of disappointment, but in fact one of optimism: As we also discussed, recent years have seen tremendous progress in understanding potential pitfalls in the application of DFT to metal–molecule interfaces and in developing successful methods to overcome them. Consequently, many applications once considered to be "too difficult for DFT" are now well within our reach. Second, the examples we have selected were, naturally, strongly biased towards the research work of the authors, as it is impossible to do full justice to the the work of many other scientists on many additional systems within the confines of this chapter. Nevertheless, we do trust that the work surveyed here provides some general lessons on structural, electronic, and magnetic properties of the molecule–metal interface, and on the importance of collective effects therein. We therefore hope it would be of benefit to both theorists and experimentalists working in this fascinating area.

References

1 Cahen, D., Kahn, A., and Umbach, E. (2005) Energetics of molecular interfaces. *Mater. Today*, **8**, 32–41.

2 Kronik, L. and Koch, N. (2010) Electronic properties of organic-based interfaces. *MRS Bull.*, **35**, 417–421.

3 Cahen, D., Naaman, R., and Vager, Z. (2005) The cooperative molecular field effect. **15**, 1571–1578.

4 Carmeli, I., Leitus, G., Naaman, R., Reich, S., and Vager, Z. (2003) The cooperative molecular field effect. *J. Chem. Phys.*, **118**, 10372–10375.

5 Temirov, R., Soubatch, S., Luican, A., and Tautz, F.S. (2006) Free-electron-like dispersion in an organic monolayer film on a metal substrate. *Nature*, **444**, 350–353.

6 Romaner, L., Heimel, G., Brédas, J.L., Gerlach, A., Schreiber, F., Johnson, R.L., Zegenhagen, J., Duhm, S., Koch, N., and Zojer, E. (2007) Impact of bidirectional charge transfer and molecular distortions on the electronic structure of a metal–organic interface. *Phys. Rev. Lett.*, **99**(25), 256801.

7 Schwalb, C.H., Sachs, S., Marks, M., Schoell, A., Reinert, F., Umbach, E., and Hoefer, U. (2008) Electron lifetime in a

Shockley-type metal–organic interface state. *Phys. Rev. Lett.*, **101**, 146801.

8 Wende, H., M. Bernien, J.L., Sorg, C., Ponpandian, N., Kurde, J., Miguel, J., Piantek, M., Xu, X., Eckhold, P., Kuch, W., Baberschke, K., Panchmatia, P.M., Sanyal, B., Oppeneer, P.M., and Eriksson, O. (2007) Substrate-induced magnetic ordering and switching of iron porphyrinmolecules. *Nat. Mater.*, **6**, 516–520.

9 Atodiresei, N., Brede, J., Lazic, P., Caciuc, V., Hoffmann, G., Wiesendanger, R., and Bluegel, S. (2010) Design of the local spin polarization at the organic-ferromagnetic interface. *Phys. Rev. Lett.*, **105**, 066601.

10 Brede, J., Atodiresei, N., Kuck, S., Lazic, P., Caciuc, V., Morikawa, Y., Hoffmann, G., Bluegel, S., and Wiesendanger, R. (2010) Spin- and energy-dependent tunneling through a single molecule with intramolecular spatial resolution. *Phys. Rev. Lett.*, **105**, 047204.

11 Agranovich, V.M., Basko, D.M., Rocca, G.C.L., and Bassani, F. (1998) Excitons and optical nonlinearities in hybrid organic–inorganic nanostructures. *J. Phys.: Cond. Matter*, **10**, 9369.

12 Blumstengel, S., Sadofev, S., Xu, C., Puls, J., and Henneberger, F. (2006) Converting wannier into frenkel excitons in an inorganic/organic hybrid semiconductor nanostructure. *Phys. Rev. Lett.*, **97**, 237401.

13 Zhu, X.Y., Yang, Q., and Muntwiler, M. (2009) Charge transfer excitons at organic semiconductor surfaces and interfaces. *Acct. Chem. Res.*, **42**, 1779.

14 Natan, A., Kronik, L., Haick, H., and Tung, R.T. (2007) Electrostatic properties of ideal and nonideal polar organic monolayers: Implications for electronic devices. *Adv. Mater.*, **19**, 4103.

15 Heimel, G., Rissner, F., and Zojer, E. (2010) Modeling the electronic properties of pi-conjugated self-assembled monolayers. *Adv. Mater.*, **22**, 2494.

16 Deutsch, D., Natan, A., Shapira, Y., and Kronik, L. (2007) Electrostatic properties of adsorbed polar molecules: Opposite behavior of a single molecule and a molecular monolayer. *J. Am. Chem. Soc.*, **129**, 2989–2997.

17 Landau, A., Kronik, L., and Nitzan, A. (2008) Cooperative effects in molecular conduction. *J. Comp. Theo. Nanosci.*, **5**, 535–544.

18 Reuter, M.G., Seideman, T., and Ratner, M.A. (2011) Molecular conduction through adlayers: Cooperative effects can help or hamper electron transport. *Nano Lett.*, **11**, 4693–4696.

19 Neaton, J.B., Hybertsen, M.S., and Louie, S.G. (2006) Renormalization of molecular electronic levels at metal–molecule interfaces. *Phys. Rev. Lett.*, **97**(21), 216405.

20 Cramer, C. (2004) *Essentials of Computational Chemistry: Theories and Models*, John Wiley & Sons, Inc, Hoboken.

21 Martin, R.M. (2004) *Electronic Structure: Basic Theory and Practical Methods*, Cambridge University Press, Cambridge.

22 Parr, R.G. and Yang, W. (1989) *Density Functional Theory of Atoms and Molecules*, Oxford University Press, Oxford.

23 Dreizler, M. and Gross, E.K.U. (1990) *Density Functional Theory: An Approach to the Quantum Many-Body Problem*, Springer, Berlin.

24 Koch, W. and Holthausen, M.C. (2001) *A Chemist's Guide to Density Functional Theory*, Wiley-VCH GmbH & Co. KGaA, Weinheim.

25 Sholl, D. and Steckel, J.A. (2009) *Density Functional Theory: A Practical Introduction*, Wiley-VCH GmbH & Co. KGaA, Weinheim.

26 Hohenberg, P. and Kohn, W. (1964) Inhomogeneous electron gas. *Phys. Rev.*, **136**(3B), B864–B871.

27 Kohn, W. and Sham, L.J. (1965) Self-consistent equations including exchange and correlation effects. *Phys. Rev.*, **140**(4A), A1133–A1138.

28 Ceperley, D.M. and Alder, B.J. (1980) Ground state of the electron gas by a stochastic method. *Phys. Rev. Lett.*, **45**, 566.

29 Vosko, S.H., Wilk, L., and Nusair, M. (1980) Accurate spin-dependent electron liquid correlation energies for local spin density calculations: A critical analysis. *Can. J. Phys.*, **58**, 1200.

30 Perdew, J.P. and Zunger, A. (1981) Self-interaction correction to density-functional approximations for many-electron systems. *Phys. Rev. B*, **23**, 5048.

31 Perdew, J.P. and Wang, Y. (1992) Accurate and simple analytic representation of the electron-gas correlation energy. *Phys. Rev. B*, **45**, 13244.

32 Yin, M.T. and Cohen, M.L. (1980) Microscopic theory of the phase transformation and lattice dynamics of si. *Phys. Rev. Lett.*, **45**, 1004.

33 Perdew, J.P. and Kurth, S. (2003) Density functionals for nonrelativistic coulomb systems in the new century, in *A Primer in Density Functional Theory* (eds C. Fiolhais, F. Nogueira, and M.A.L. Marques), Springer, Berlin, pp. 1–55.

34 Perdew, J.P., Burke, K., and Ernzerhof, M. (1996) Generalized gradient approximation made simple. *Phys. Rev. Lett.*, **77**(18), 3865.

35 Becke, A.D. (1988) Correlation energy of an inhomogeneous electron gas: a coordinate space model. *J. Chem. Phys.*, **88**, 1053.

36 Kümmel, S. and Kronik, L. (2008) Orbital-dependent density functionals: Theory and applications. *Rev. Mod. Phys.*, **80**(1), 3–60.

37 Stephens, P.J., Devlin, F.J., Chabalowski, C.F., and Frisch, M.J. (1994) Ab initio calculation of vibrational absorption and circular dichroism spectra using density functional force fields. *J. Phys. Chem.*, **98**, 11623.

38 Seidl, A., Goerling, A., Vogl, P., Majewski, J.A., and Levy, M. (1996) Generalized Kohn–Sham schemes and the band-gap problem. *Phys. Rev. B*, **53**, 3764.

39 Baer, R., Livshits, E., and Salzner, U. (2010) Tuned range-separated hybrids in density functional theory. *Annu. Rev. Phys. Chem.*, **61**, 85–109.

40 Kronik, L., Stein, T., Refaely-Abramson, S., and Baer, R. (2012) Excitation gaps of finite-sized systems from optimally tuned range-separated hybrid functionals. *J. Chem. Theory. Comput.*, **8**, 1515–1531.

41 Staroverov, V.N., Scuseria, G.E., Tao, J., and Perdew, J.P. (2003) Comparative assessment of a new nonempirical density functional: Molecules and hydrogen-bonded complexes. *J. Chem. Phys.*, **119**, 12129.

42 Leininger, T., Stoll, H., Werner, H.J., and Savin, A. (1997) Combining long-range configuration interaction with short-range density functionals. *Chem. Phys. Lett.*, **275**, 151–160.

43 Bylander, D.M. and Kleinman, L. (1990) Good semiconductor bandgaps with a modified local-density approximation. *Phys. Rev. B*, **41**, 7868.

44 Gill, P.M., Adamson, R.D., and Pople, J.A. (1996) Coulomb-attenuated exchange energy density functionals. *Mol. Phys.*, **88**, 1005–1009.

45 Heyd, J., Scuseria, G.E., and Ernzerhof, M. (1993) Hybrid functionals based on a screened coulomb potential. *J. Chem. Phys.*, **118**, 8207.

46 Krukau, A.V., Vydrov, O.A., Izmaylov, A.F., and Scuseria, G.E. (1996) Influence of the exchange screening parameter on the performance of screened hybrid functionals. *J. Chem. Phys.*, **125**, 224106.

47 Levy, M., Perdew, J.P., and Sahni, V. (1984) Exact differential equation for the density and ionization energy of a many particle system. *Phys. Rev. A*, **30**, 2745.

48 Almbladh, C.O. and von Barth, U. (1985) Exact results for the charge and spin densities, exchange–correlation potentials, and density-funcitonal eigenvalues. *Phys. Rev. B*, **31**, 3231.

49 Chong, D.P., Gritsenko, O.V., and Baerends, E.J. (2002) Interpretation of the Kohn–Sham orbital energies as approximate vertical ionization potentials. *J. Chem. Phys.*, **116**, 1760.

50 Jones, R.O. and Gunnarsson, O. (1989) The density functional formalism, its applications and prospects. *Rev. Mod. Phys.*, **61**, 689.

51 Dauth, M., Koerzdoerfer, T., Kuemmel, S., Ziroff, J., Wiessner, M., Schoell, A., Reinert, F., Arita, M., and Shimada, K. (2011) Orbital density reconstruction for molecules. *Phys. Rev. Lett.*, **107**, 193002.

52 Puschnig, P., Reinisch, E.M., Ules, T., Koller, G., Soubatch, S., Ostler, M., Romaner, L., Tautz, F.S., Ambrosch-Draxl, C., and Ramsey, M.G. (2011) Orbital tomography: Deconvoluting photoemis-

sion spectra of organic molecules. *Phys. Rev. B*, **84**, 235427.

53 Dion, M., Rydberg, H., Schröder, E., Langreth, D.C., and Lundqvist, B.I. (2004) Van der Waals density functional for general geometries. *Phys. Rev. Lett.*, **92**(24), 246401.

54 Langreth, D.C., Lundqvist, B.I., Chakarova-Käck, S.D., Cooper, V.R., Dion, M., Hyldgaard, P., Kelkkanen, A., Kleis, J., Kong, L., Li, S., Moses, P.G., Murray, E., Puzder, A., Rydberg, H., Schröder, E., and Thonhauser, T. (2009) A density functional for sparse matter. *J. Phys.: Condens. Matter*, **21**(8), 084203.

55 Lee, K., Murray, E.D., Kong, L., Lundqvist, B.I., and Langreth, D.C. (2010) Higher-accuracy van der Waals density functional. *Phys. Rev. B*, **82**, 081101.

56 Vydrov, O.A. and Voorhis, T.V. (2010) Nonlocal van der Waals density functional: The simpler the better. *J. Chem. Phys.*, **133**, 244103.

57 Grimme, S. (2006) Semiempirical GGA-type density functional constructed with a long-range dispersion correction. *J. Comput. Chem.*, **27**(15), 1787–1799.

58 Grimme, S., Antony, J., Ehrlich, S., and Krieg, H. (2010) A consistent and accurate ab initio parameterzation of density functional dispersion correction (DFT-D) for the 94 elements H-PU. *J. Chem. Phys.*, **132**(15), 154104.

59 Tkatchenko, A. and Scheffler, M. (2009) Accurate molecular van der Waals interactions from ground state electron density and free-atom reference data. *Phys. Rev. Lett.*, **102**(7), 073005.

60 Ruiz, V.G., Liu, W., Zojer, E., Scheffler, M., and Tkatchenko, A. (2012) Density-functional theory with screened van der Waals interactions for the modeling of hybrid inorganic–organic systems. *Phys. Rev. Lett.*, **108**, 146103.

61 Marom, N., Tkatchenko, A., Scheffler, M., and Kronik, L. (2010) Describing both dispersion interactions and electronic structure using density functional theory: The case of metal-phthalocyanine dimers. *J. Chem. Theory Comput.*, **6**, 81–90.

62 Marom, N., Tkatchenko, A., Rossi, M., Gobre, V.V., Hod, O., Scheffler, M., and Kronik, L. (2011) Dispersion interactions with density-functional theory: Benchmarking semiempirical and interatomic pairwise corrected density functionals. *J. Chem. Theory Comput.*, **7**, 3944–3951.

63 Zhao, Y. and Truhlar, D.G. (2008) The M06 suite of density functionals for main group thermochemistry, thermochemical kinetics, noncovalent interactions, excited states, and transition elements: two new functionals and systematic testing of four M06-class functionals and 12 other functionals. *Theor. Chem. Accounts*, **120**, 215–241.

64 Zhao, Y. and Truhlar, D.G. (2008) Density functionals with broad applicability in chemistry. *Acct. Chem. Res.*, **41**, 157–167.

65 Ferrighi, L., Madsen, G.K.H., and Hammer, B. (2011) Self-consistent meta-generalized gradient approximation study of adsorption of aromatic molecules on noble metal surfaces. *J. Chem. Phys.*, **135**, 084704.

66 Paier, J., Marsman, M., and Kresse, G. (2007) Why does the b3lyp hybrid functional fail for metals? *J. Chem. Phys.*, **127**, 024103.

67 Umbach, E., Seidel, C., Taborski, J., Li, R., and Soukopp, A. (1995) Highly ordered organic adsorbates: Commensurate superstructures, OMBE, and 1d nanostructures. *Phys. Status Solidi (b)*, **192**, 389–406.

68 Dori, N., Menon, M., Kilian, L., Sokolowski, M., Kronik, L., and Umbach, E. (2006) Valence electronic structure of gas phase 3,4,9,10-perylene tetracarboxylic-acid-dianhydride (PTCDA): Experiment and theory. *Phys. Rev. B*, **73**, 195208.

69 Hybertsen, M.S. and Louie, S.G. (1986) Electron correlation in semiconductors and insulators: Bandgaps and quasiparticle energies. *Phys. Rev. B*, **34**, 5390.

70 Körzdörfer, T., Kümmel, S., Marom, N., and Kronik, L. (2009) When to trust photoelectron spectra from Kohn–Sham eigenvalues: The case of organic semiconductors. *Phys. Rev. B*, **79**(20), 201205(R).

71 Marom, N., Ren, X., Moussa, J.E., Chelikowsky, J.R., and Kronik, L. (2011) Electronic structure of copper phthalocyanine from G_0W_0 calculations. *Phys. Rev. B*, **84**, 195143.

72 Evangelista, F., Carravetta, V., Stefani, G., Jansik, B., Alagia, M., Stranges, S., and Ruocco, A. (2007) Electronic structure of copper phthalocyanine: An experimental and theoretical study of occupied and unoccupied levels. *J. Chem. Phys.*, **126**, 124709.

73 Murdey, R., Sato, N., and Bouvet, M. (2006) Electronic structure of copper phthalocyanine: An experimental and theoretical study of occupied and unoccupied levels. *Mol. Cryst. Liq. Cryst.*, **455**, 211–218.

74 Hill, I., Kahn, A., Soos, Z., and Pascal, R. (2000) Charge-separation energy in films of pi-conjugated organic molecules. *Chem. Phys. Lett.*, **327**, 181–188.

75 Paier, J., Marsman, M., Hummer, K., Kresse, G., Gerber, I.C., and Angyan, J.G. (2006) Screened hybrid density functionals applied to solids. *J. Chem. Phys.*, **124**, 154709.

76 Marom, N., Hod, O., Scuseria, G.E., and Kronik, L. (2008) Electronic structure of copper phthalocyanine: a comparative density functional theory study. *J. Chem. Phys.*, **128**, 164107.

77 Bisti, F., Stroppa, A., Donarelli, M., Picozzi, S., and Ottaviano, L. (2011) Electronic structure of tris(8-hydroxyquinolinato)aluminium(iii) revisited using the Heyd–Scuseria–Ernzerhof hybrid functional: Theory and experiments. *Phys. Rev. B*, **84**, 195112.

78 Biller, A., Tamblyn, I., Neaton, J.B., and Kronik, L. (2011) Electronic level alignment at a metalmolecule interface from a short-range hybrid functional. *J. Chem. Phys.*, **135**, 164706.

79 Stein, T., Eisenberg, H., Kronik, L., and Baer, R. (2010) Fundamental gaps of finite systems from the eigenvalues of a generalized Kohn–Sham method. *Phys. Rev. Lett.*, **105**, 266802.

80 Refaely-Abramson, S., Baer, R., and Kronik, L. (2011) Fundamental and excitation gaps in molecules of relevance for organic photovoltaics from an optimally tuned range-separated hybrid functional. *Phys. Rev. B*, **84**, 075144.

81 Kronik, L., Stein, T., Refaely-Abramson, S., and Baer, R. (2012) Excitation gaps of finite-sized systems from optimally-tuned range-separated hybrid functionals. *J. Chem. Theo. Comp.*, **8**, 1515.

82 Magid, I., Burstein, L., Seitz, O., Segev, L., Kronik, L., and Rosenwaks, Y. (2008) Electronic characterization of Si(100)-bound alkyl monolayers using kelvin probe force microscopy. *J. Phys. Chem. C*, **112**, 7145–7150.

83 Track, A.M., Rissner, F., Heimel, G., Romaner, L., Kafer, D., Bashir, A., Rannger, G.M., Hofmann, O.T., Bucko, T., Witte, G., and Zojer, E. (2010) Simultaneously understanding the geometric and electronic structure of anthraceneselenolate on Au(111): A combined theoretical and experimental study. *J. Phys. Chem. C*, **114**, 2677–2684.

84 Fatemi, V., Kamenetska, M., Neaton, J.B., and Venkataraman, L. (2011) Environmental control of single-molecule junction transport. *Nano Lett.*, **11**, 1988–1992.

85 Ishii, H., Sugiyama, K., Ito, E., and Seki, K. (1999) Energy level alignment and interfacial electronic structures at organic/metal and organic/organic interfaces. *Adv. Mater.*, **11**(8), 605–625.

86 Lang, N.D. (1981) Interaction between closed-shell systems and metal surfaces. *Phys. Rev. Lett.*, **46**(13), 842.

87 Bagus, P.S., Staemmler, V., and Wöll, C. (2002) Exchange-like effects for closed-shell adsorbates: Interface dipole and work function. *Phys. Rev. Lett.*, **89**(9), 096104.

88 Sze, S.M. and Ng, K.K. (2006) *Physics of Semiconductor Devices*, 3rd edn, John Wiley & Sons, Inc, New York.

89 Vázquez, H., Qszwaldowski, R., Pou, P., Ortega, J., Pérez, R., Flores, F., and Kahn, A. (2004) Dipole formation at metal/PTCDA interfaces: Role of the charge neutrality level. *Europhys. Lett.*, **65**(6), 802–808.

90 Vázquez, H., Qszwaldowski, R., Ortega, J., Pérez, R., and Kahn, A. (2004) Barrier formation at metal–organic interfaces: dipole formation and the charge neu-

trality level. *Appl. Surf. Sci.*, **234**(1–4), 107–112.

91 Vázquez, H., Gao, W., Flores, F., and Kahn, A. (2005) Energy level alignment at organic heterojunctions: Role of the charge neutrality level. *Phys. Rev. B*, **71**(4), 041306.

92 Vázquez, H., Flores, F., and Kahn, A. (2007) Induced density of states model for weakly-interacting organic semiconductor interfaces. *Org. Electron.*, **8**(2–3), 241–248.

93 Vázquez, H., Dappe, Y.J., Ortega, J., and Flores, F. (2007) Energy level alignment at metal/organic semiconductor interfaces: "Pillow" effect, induced density of interface states, and charge neutrality level. *J. Chem. Phys.*, **126**(14), 144703.

94 Morikawa, Y., Ishii, H., and Seki, K. (2004) Theoretical study of *n*-alkane adsorption on metal surfaces. *Phys. Rev. B*, **69**(4), 041403.

95 Caputo, R., Prascher, B.P., Staemmler, V., Bagus, P.S., and Wöll, C. (2007) Adsorption of benzene on coinage metals: A theoretical analysis using wavefunction-based methods. *J. Phys. Chem. A*, **111**(49), 12778–12784.

96 Bagus, P.S., Hermann, K., and Wöll, C. (2005) The interaction of C_6H_6 and C_6H_{12} with noble metal surfaces: Electronic level alignment and the origin of the interface dipole. *J. Chem. Phys.*, **123**(18), 184109.

97 Witte, G., Lukas, S., Bagus, P.S., and Wöll, C. (2005) Vacuum level alignment at organic/metal junctions: 'cushion' effect and the interface dipole. *Appl. Phys. Lett.*, **87**(26), 263502.

98 Koschel, H., Held, G., and Steinruck, H.P. (1999) The orientation of benzene on bimetallic surfaces. *Surf. Rev. Lett.*, **6**(5), 893–901.

99 Zhou, X.L., Castroa, M.E., and Whitea, J.M. (1990) Interactions of UV photons and low-energy electrons with chemisorbed benzene on Ag(111). *Surf. Sci.*, **238**(1–3), 215–225.

100 Lukas, S. (2006) Ph.D. dissertation, Faculty for Chemistry, Rhur-University, Bochum.

101 Dudde, R., Frank, K.H., and Koch, E.E. (1990) The electronic structure of benzene adsorbed on Ag(111) studied by angle resolved photoemission. *Surf. Sci.*, **225**(3), 267–272.

102 Rockey, T.J., Yang, M., and Dai, H.L. (2006) Adsorption energies, interadsorbate interactions, and the two binding sites within monolayer benzene on Ag(111). *J. Phys. Chem. B*, **110**(40), 19973–19978.

103 Triguero, L., Pettersson, L.G.M., Minaev, B., and Ågren, H. (1998) Spin uncoupling in surface chemisorption of unsaturated hydrocarbons. *J. Chem. Phys.*, **108**(3), 1193–1205.

104 Bilić, A., Reimers, J.R., Hush, N.S., Hoft, R.C., and Ford, M.J. (2006) Adsorption of benzene on copper, silver, and gold surfaces. *J. Chem. Theory Comput.*, **2**(4), 1093–1105.

105 Munakata, T., Sakashita, T., Tsukakoshi, M., and Nakamura, J. (1997) Fine structure of the two-photon photoemission from benzene adsorbed on Cu(111). *Chem. Phys. Lett.*, **271**(4–6), 377–380.

106 Munakata, T. (1999) Dispersion of an adsorption-induced electronic state of benzene/Cu(111). *J. Chem. Phys.*, **110**(5), 2736–2737.

107 Munakata, T. (2000) Bonding state formed between adsorbed benzene and Cu(111). *Surf. Sci.*, **454–456**(20), 118–121.

108 Sonoda, Y. and Munakata, T. (2007) Occupied and unoccupied electronic states of benzene adsorbed Cu(110) surface. *Chem. Phys. Lett.*, **445**(4–6), 198–202.

109 Lorente, N., Hedouin, M.F.G., Palmer, R.E., and Persson, M. (2007) Chemisorption of benzene and stm dehydrogenation products on Cu(100). *Phys. Rev. B*, **68**(15), 155401.

110 Han, P., Mantooth, B.A., Sykes, E.C.H., Donhauser, Z.J., and Weiss, P.S. (2004) Benzene on Au{111} at 4 K: Monolayer growth and tip-induced molecular cascades. *J. Am. Chem. Soc.*, **126**(34), 10787–10793.

111 Tsuzuki, S., Honda, K., Uchimaru, T., Mikami, M., and Tanabe, K. (2002) Origin of attraction and directionality of the π/π interaction: Model chemistry calculations of benzene dimer interaction. *J. Am. Chem. Soc.*, **124**(1), 104–112.

112 Tsuzuki, S., Honda, K., Uchimaru, T., and Mikami, M. (2004) High-level *ab initio* computations of structures and interaction energies of naphthalene dimers: Origin of attraction and its directionality. *J. Chem. Phys.*, **120**(2), 647–659.

113 Toyoda, K., Nakano, Y., Hamada, I., Lee, K., Yanagisawa, S., and Morikawa, Y. (2009) First-principles study of benzene on noble metal surfaces: Adsorption states and vacuum level shifts. *Surf. Sci.*, **603**(18), 2912–2922.

114 Toyoda, K., Hamada, I., Yanagisawa, S., and Morikawa, Y. (2011) Adsorption of benezene on noble metal surfaces studied by density functional theory with van der Waals correction. *J. Nanosci. Nanotechnol.*, **11**, 2836.

115 McNellis, E., Meyer, J., and Reuter, K. (2009) Azobenzene at coinage metal surfaces: The role of dispersive van der Waals interactions. *Phys. Rev. B*, **80**(20), 205414.

116 Romaner, L., Nabok, D., Puschnig, P., Zojer, E., and Ambrosch-Draxl, C. (2009) Theoretical study of PTCDA adsorbed on the coinage metal surfaces, Ag(111), Au(111) and Cu(111). *New J. Phys.*, **11**(5), 053010.

117 Somorjai, G.A. (1994) *Introduction to Surface Chemistry and Catalysis*, Chapt. 7, John Wiley & Sons, Inc., New York, p. 442.

118 Koch, N., Salzmann, I., Johnson, R.L., Pflaum, J., Friedlein, R., and Rabe, J. (2006) Molecular orientation dependent energy levels at interfaces with pentacene and pentacenequinone. *Org. Electron.*, **7**(6), 537–545.

119 Koch, N., Vollmer, A., Duhm, S., Sakamoto, Y., and Suzuki, T. (2007) The effect of fluorination on pentacene/gold interface energetics and charge reorganization energy. *Adv. Mater.*, **19**(1), 112–116.

120 Ferretti, A., Baldacchini, C., Calzolari, A., Felice, R.D., Ruini, A., Molinari, E., and Betti, M.G. (2007) Mixing of electronic states in pentacene adsorption on copper. *Phys. Rev. Lett.*, **99**(4), 046802.

121 Yamane, H., Yoshimura, D., Kawabe, E., Sumii, R., Kanai, K., Ouchi, Y., Ueno, N., and Seki, K. (2007) Electronic structure at highly ordered organic/metal interfaces: Pentacene on Cu(110). *Phys. Rev. B*, **76**(16), 165436.

122 Käfer, D. and Witte, G. (2007) Evolution of pentacene films on Ag(111): Growth beyond the first monolayer. *Chem. Phys. Lett.*, **442**(4–6), 376–383.

123 Yamane, H., Kawabe, E., Yoshimura, D., Sumii, R., Kanai, K., Ouchi, Y., Ueno, N., and Seki, K. (2008) Intermolecular band dispersion in highly ordered monolayer and multilayer films of pentacene on Cu(110). *Phys. Stat. Solidi (b)*, **245**(5), 793–798.

124 Koch, N., Gerlach, A., S. Duhm, H.G., G. Heimel, A.V., Sakamoto, Y., Suzuki, T., Zegenhagen, J., Rabe, J.P., and Schreiber, F. (2008) Adsorption-induced intramolecular dipole: Correlating molecular conformation and interface electronic structure. *J. Am. Chem. Soc.*, **130**(23), 7300–7304.

125 Dougherty, D.B., Jin, W., Cullen, W.G., Reutt-Robey, J.E., and Robey, S.W. (2008) Variable temperature scanning tunneling microscopy of pentacene monolayer and bilayer phases on Ag(111). *J. Phys. Chem. C*, **112**(51), 20334–20339.

126 Simeoni, M., Picozzi, S., and Delley, B. (2004) An ab-initio study of pentacene on aluminum (100) surface. *Surf. Sci.*, **562**(1–3), 43.

127 Lee, K. and Yu, J. (2005) Ab initio study of pentacene on Au(001) surface. *Surf. Sci.*, **589**(1–3), 8–18.

128 Lee, K., Yu, J., and Morikawa, Y. (2007) Comparison of the localized basis and plane-wave basis for density functional calculations of organic molecules on metals. *Phys. Rev. B*, **75**(4), 045402.

129 Toyoda, K., Nakano, Y., Hamada, I., Lee, K., Yanagisawa, S., and Morikawa, Y. (2009) First-principles study of the pentacene/Cu(111) interface: Adsorption states and vacuum level shifts. *J. Electron Spectrosc. Relat. Phenom.*, **174**(1–3), 78–84.

130 Toyoda, K., Hamada, I., Yanagisawa, S., and Morikawa, Y. (2010) Origin of surface-band dispersion at the pentacene/Cu interface. *Appl. Phys. Exp.*, **3**, 025701-1–3.

131 Toyoda, K., Hamada, I., Lee, K., Yanagisawa, S., and Morikawa, Y. (2010) Density functional theoretical study of pentacene/noble metal interfaces with van der Waals corrections: Vacuum level shifts and electronic structures. *J. Chem. Phys.*, **132**(13), 134703.

132 Schroeder, P.G., France, C.B., Park, J.B., and Parkinson, B.A. (2002) Energy level alignment and two-dimensional structure of pentacene on Au(111) surfaces. *Appl. Phys. Lett.*, **91**(5), 3010–3014.

133 Forrest, S.R. (1997) Ultrathin organic films grown by organic molecular beam deposition and related techniques. *Chem. Rev.*, **97**, 1793–1896.

134 Glöckler, K., Seidel, C., Soukopp, A., Sokolowski, M., Umbach, E., Böhringer, M., Berndt, R., and Schneider, W.D. (1998) Highly ordered structures and sub molecular scanning tunnelng microscopy contrast of PTCDA and DM-PBDCI monolayers on Ag(111) and Ag(110). *Surf. Sci.*, **405**, 1–20.

135 Tautz, F. (2007) Structure and bonding of large aromatic molecules on noble metal surfaces: The example of PTCDA. *Prog. Surf. Sci.*, **82**, 479–520.

136 Hauschild, A., Karki, K., Cowie, B., Rohlfing, M., Ta utz, F., and Sokolowski, M. (2005) Molecular distortions and chemical bonding of a large π-conjugated molecule on a metal surface. *Phys. Rev. Lett.*, **94**(3), 036106.

137 Du, S., Gao, H., Seidel, C., Tsetseris, L., Ji, W., Kopf, H., Chi, L., Fuchs, H., Pennycook, S., and Pantelides, S. (2006) Selective nontemplated adsorption of organic molecules on nanofacets and role of bonding patterns. *Phys. Rev. Lett.*, **97**(15), 156105.

138 Rohlfing, M. and Bredow, T. (2008) Binding energy of adsorbates on a noble-metal surface: Exchange and correlation effects. *Phys. Rev. Lett.*, **101**(26), 266106.

139 Ziroff, J., Forster, F., Schöll, A., Puschnig, P., and Reinert, F. (2010) Hybridization of organic molecular orbitals with substrate states at interfaces: PTCDA on silver. *Phys. Rev. Lett.*, **104**(23), 233004.

140 Rusu, P.C., Giovannetti, G., Weijtens, C., Coehoorn, R., and Brocks, G. (2010) First-principles study of the dipole layer formation at metal–organic interfaces. *Phys. Rev. B*, **81**(12), 125403.

141 Ohto, T., Yamashita, K., and Nakamura, H. (2011) First-principles study of electronic structure and charge transport at PTCDA molecular layers on Ag(111) and Al(111) electrodes. *Phys. Rev. B*, **84**(12), 045417.

142 Martínez, J., Abad, E., Flores, F., Ortega, J., and Brocks, G. (2011) Barrier height formation for the PTCDA/Au(111) interface. *Chem. Phys.*, **390**, 14–19.

143 Rurali, R., Lorente, N., and Ordejón, P. (2005) Comment on molecular distortions and chemical bonding of a large π-conjugated molecule on a metal surface. *Phys. Rev. Lett.*, **95**(20), 209601.

144 Hauschild, A., Karki, K., Cowie, B., Rohlfing, M., Tautz, F., and Sokolowski, M. (2005) Reply. *Phys. Rev. Lett.*, **95**(20), 209602.

145 Egger, D.A., Rissner, F., Rangger, G.M., Hofmann, O.T., Wittwer, L., Heimel, G., and Zojer, E. (2010) Self-assembled monolayers of polar molecules on au(111) surfaces: distributing the dipoles. *Phys. Chem. Chem. Chem. Phys.*, **12**, 4291–4294.

146 Rissner, F., Egger, D.A., Natan, A., Körzdörfer, T., Kümmel, S., Kronik, L., and Zojer, E. (2011) Collectively induced quantum-confined Stark effect in monolayers of molecules consisting of polar repeating units. *J. Am. Chem. Soc.*, **133**, 18634–18645.

147 Rissner, F., Natan, A., Egger, D.A., Hofmann, O.T., Kronik, L., and Zojer, E. (2012) Dimensionality effects in the electronic structure of organic semiconductors consisting of polar repeat units. *Org. Electron.*, **13**, 3165–3176.

148 Miller, D.A.B., Chemla, D.S., Damen, T.C., Gossard, A.C., Wiegmann, W., Wood, T.H., and Burrus, C.A. (1984) Band-edge electroabsorption in quantum well structures: The quantum-confined stark effect. *Phys. Rev. Lett.*, **53**, 2173–2176.

149 Marom, N. and Kronik, L. (2009) Density functional theory of transition metal phthalocyanines, I: electronic structure

of NIPC and COPC—self-interaction effects. *Appl. Phys. A*, **95**, 159–163.
150 Schultz, B.D., Marom, N., Naveh, D., Lou, X., Adelmann, C., Strand, J., Crowell, P.A., Kronik, L., and Palmstrom, C.J. (2009) Spin injection across the Fe/GaAs interface: Role of interfacial ordering. *Phys. Rev. B*, **80**, 201309(R).